Ubiquitin ligases Siah1a/2 control alveolar macrophage functions to limit carcinogen-induced lung adenocarcinoma

Marzia Scortegagna[1,^], **Yuanning Du**[1], **Linda M. Bradley**[1], **Kun Wang**[2], **Alfredo Molinolo**[3], **Eytan Ruppin**[2], **Rabi Murad**[1], **Ze'ev A. Ronai**[1,^]

[1]NCI-designated Cancer Center, Sanford Burnham Prebys Medical Discovery Institute, La Jolla CA,

[2]Cancer Data Science Laboratory, National Cancer Institute, National Institutes of Health, Bethesda, MD,

[3]Department of Pathology, University of California San Diego, CA.

Abstract

Cellular components of the tumor microenvironment, including myeloid cells, play important roles in the progression of lung adenocarcinoma (LUAD) and its response to therapy. Here, we characterize the function of the ubiquitin ligases Siah1a/2 in regulating the differentiation and activity of alveolar macrophages (AMs) and assess the implication of Siah1a/2 control of AMs for carcinogen-induced LUAD. Macrophage-specific genetic ablation of Siah1a/2 promoted accumulation of AMs with an immature phenotype and increased expression of pro-tumorigenic and pro-inflammatory Stat3 and β-catenin gene signatures. Administration of urethane to wild-type mice promoted enrichment of immature-like AMs and lung tumor development, which was enhanced by macrophage-specific Siah1a/2 ablation. The pro-fibrotic gene signature seen in Siah1a/2-ablated immature-like macrophages was associated with increased tumor infiltration of CD14+ myeloid cells and poorer survival of LUAD patients. Single-cell RNA-seq confirmed the presence of a cluster of immature-like AMs expressing a pro-fibrotic signature in lungs of LUAD patients, a signature enhanced in smokers. These findings identify Siah1a/2 in alveolar macrophages as gatekeepers of lung cancer development.

Keywords

Siah1a; Siah2; macrophages; alveolar macrophages; lung cancer; urethane; lung adenocarcinoma; β-catenin

Introduction

Recognition of the crucial role played by the immune system in controlling tumor initiation, progression, and response to therapy has prompted the development of therapies that exploit the activity of immune cells and mediators (1,2). The tumor microenvironment (TME) components participate in extensive crosstalk that regulates immune cell activation and tumor infiltration. Within the TME, various immune cells control tumor growth: some, such as cytotoxic and regulatory T cells and dendritic cells (DCs), are well studied (3,4), while the contributions of fibroblasts, endothelial cells, and myeloid cells, including macrophages, to tumor growth control are less well understood (5,6).

Approximately 85% of lung cancers are non-small cell lung cancers, of which lung adenocarcinoma (LUAD) and squamous cell carcinoma are the most common subtypes (7). In response to chemical carcinogens (e.g., urethane), mice develop pulmonary adenocarcinoma marked by KRAS mutations and resembling human LUAD (8). Several studies report the importance of the TME to lung cancer development, including immune system components such as macrophages, and their possible contribution to cancer development (9,10). Two macrophage populations reside in normal lung tissues: alveolar macrophages (AMs), which are in close contact with type I and II epithelial cells in alveoli, and interstitial macrophages (IMs), which reside in the parenchyma between the vascular endothelium and the alveolar epithelium (11,12). AMs are derived from fetal monocytes that populate alveoli after birth and self-renew outside of the bone marrow (13). Fetal monocytes accumulate in developing mouse lung at embryonic day 14.5 (E14.5) and differentiate into immature fetal AMs ($CD11b^{int}$ $F4/80^+$ $CD11c^{int}$ $SiglecF^-$) (14,15), which then further differentiate postnatally into immature ($CD11b^{low}$ $F4/80^+$ $CD11c^+$ $SiglecF^-$) and mature ($CD11b^{low}$ $F4/80^+$ $CD11c^+$ $SiglecF^+$) AMs. Postnatal differentiation requires signaling *via* the growth factor granulocyte/macrophage-colony-stimulating factor (GM-CSF) and the ligand-activated transcription factor peroxisome proliferator-activated receptor-γ (PPARγ) (16). Although AMs self-renew under physiological conditions, they can differentiate from bone marrow (BM)-derived monocytes following an inflammatory insult or infection (13). AM development and function during acute infection or chronic inflammation are modulated by microenvironmental factors, including oxygen tension, glucose supply, exposure to surfactant-rich fluid, and communication with alveolar epithelial cells (17). Previous studies showed inverse correlations between survival of lung cancer patients and density of tumor-associated macrophages (TAMs), their abundance in stroma, and their polarization to a pro-tumorigenic phenotype (10). AMs obtained by bronchoalveolar lavage of patients with lung cancer exhibit reduced phagocytic capabilities (18), but their role in lung cancer progression remains unclear.

The importance of ubiquitin ligases in cancer development and progression is well established (19,20). Notably, transcript levels of ubiquitin ligases are largely unaltered in pathologies, including cancer, and thus are not traceable in RNA-based databases (19). Furthermore, ubiquitin ligase proteins are expressed at very low levels, given their propensity to auto-ubiquitinate and self-degrade (21). The Siah1a/2 ubiquitin ligase family has been studied in cancer primarily due to their importance in controlling hypoxia and unfolded protein response (UPR) signaling (22,23). Accordingly, Siah1a/2 were shown

to function in development of more aggressive forms of prostate cancer and melanoma, among other tumors (24,25). Notably, while Siah2 is described as an oncogene in most tumors where it is upregulated at the protein levels (including lung cancer), in select tumor types Siah1 levels decrease, suggesting it may function as a tumor suppressor in some contexts (26–30). Tumor-intrinsic roles of Siah1a/2 have been shown to be complementary in melanoma and prostate cancers (24,25).

As previously described (31), Siah1a/2 may regulate the TME. *Siah2* deletion in mice decreases melanoma tumor growth *via* Siah2-dependent regulation of T cells, primarily T regulatory cell (Treg) proliferation and tumor infiltration (31). Likewise, treatment of *Siah2*-knockout (*Siah2*^KO) mice with anti-PD1 therapy effectively blocks development of therapy-resistant ("cold") melanoma (31). These observations confirm the importance of Siah2 activity in the TME and extend our earlier analysis of Siah2 tumor-intrinsic function showing relative enrichment of macrophage subpopulations in melanomas from *Siah2*^KO mice (31).

Here, given the homology of Siah1a and Siah2 proteins (32), we analyzed their function in lung in both physiological and pathological settings using mouse models in which *Siah1a/2* genes were specifically deleted in macrophages. *Siah1a/2*^KO AMs exhibited an immature-like phenotype and expressed a pro-fibrotic gene signature enhanced following administration of the lung carcinogen urethane. Moreover, lung tumors were more abundant and larger in urethane-treated *Siah1a/2*^KO compared to WT mice. Importantly, tumor tissues from LUAD patients exhibited increased frequency of immature-like AMs as well as comparable pro-fibrotic gene signatures, outcomes more prominent in patients who were smokers compared with non- or ex- smokers. Collectively, these findings suggest that Siah1a/2 serve as gatekeepers of macrophage maturation and function in control of lung cancer development.

Material and Methods

Animals and tumor model

All experimental animal procedures were approved by the Institutional Animal Care and Use Committee of Sanford Burnham Prebys Medical Discovery Institute. *Siah1a^f/f and Siah2^f/f* mice were generated by Cyagen. *Lyz2^Cre* and *Cd11c^Cre* mice were purchased from Jackson Laboratories. All mice were on a C57BL/6 genetic background. For the urethane-induced lung cancer model, 6 to 8-week-old male mice were injected intraperitoneally with urethane (Sigma; 1 mg/g body weight) once a week for 6 weeks, and lungs were collected at either 7 or 24 weeks after the first urethane injection. Male mice, unless specified otherwise, were used to obtain animal data in this manuscript and are representative of at least three independent cohorts.

Bone marrow chimeras

C57BL/6 recipient mice were lethally irradiated (1000 rads) and reconstituted by intravenous injection of 1×10^7 BM cells isolated from femurs and tibias of donor mice, consisting of a 1:1 mixture of either WT *CD45.1*^+ cells plus WT *CD45.2*^+ cells,

or WT *CD45.1*^{+} cells plus *Siah1a/2*[f/f]*::Lyz2*[Cre] *CD45.2*^{+} cells. Recipients were treated with antibiotics (trimethoprim 8 mg/ml and sulfamethoxazole 40 mg/ml in drinking water) for 3 weeks after injection. Reconstitution was confirmed 6–8 weeks after BM transfer by FACS analysis of peripheral blood samples.

Tissue digestion

As previously reported (31) tissues were excised, minced, and digested with 1 mg/ml collagenase D (Roche) and 100 μg/ml DNase I (Sigma) at 37°C for 45 min. Digests were then passed through a 70-μm cell strainer to generate a single-cell suspension. Cells were washed twice with phosphate-buffered saline (PBS) containing 2 mM EDTA and stained for flow cytometry.

Flow cytometry

Tissue-derived single-cell suspensions were washed twice with FACS staining buffer, fixed for 15 min with 1% formaldehyde in PBS, washed twice in PBS, resuspended in FACS staining buffer, stained with appropriate antibodies, fixed with 1% formaldehyde, and analyzed by flow cytometry. For every flow cytometric antibody used, we employed Fluorescent Minus One (FMO), to distinguish positive from negative cells. The following antibodies were used and purchased from BioLegend: CD45.2 (clone 104), CD8a (53–6.7), CD4 (GK1.5), CD45.1 (A20), CD11c (N418), CD11b (M1/70), MHC class I (AF6–88.5), CD80 (16–10A1), GR1 (RB6–8C5), CD206 (C068C2), F4/80 (BM8), SiglecF (S17007L), Ly6C (HK1.4), Ly6G (1A8), NK1.1 (PK136), B220 (RA3–6B2), and CD44 (IM7). All data were collected on an LSRFortessa cytometer (BD Biosciences) and analyzed using FlowJo Software (Tree Star).

Histology and immunofluorescence

As previously reported (31) tissues (lungs) were collected and fixed in 4% formalin (overnight at 4°C), washed with PBS and paraffin-embedded before they were cut into 5 μm-thick sections and subjected to H&E staining. For immunofluorescence, sections were deparaffinized, rehydrated and washed in PBS. Antigen retrieval was performed in a pressure cooker (Decloaking chamber, Biocare Medical) in citrate buffer (pH 6.0). Antibodies against CD206 (B&D Systems AF2535), CD11c (Cell Signaling 97858) Ki67 (AbCam Ab16667), Vimentin (Cell Signaling 5741), Galectin3 (Santa Cruz Biotechnology sc-23938) and TTF1 (Novus NBP2–32999) were used for immunostaining by incubating sections overnight at 4°C with antibodies (diluted in Dako antibody diluent). Alexa Fluor 488- or Alexa Fluor 594-conjugated secondary antibodies were added for 2h at room temperature (Molecular Probes), and nuclei were counterstained using SlowFade Gold Antifade reagent (Vector) using 4′,6-diamidino-2-phenylindole (DAPI, Vector). Image data were obtained using an Olympus TH4–100 microscope and Slidebook 4.1 software. For quantification, Ki67-, Lag3- and Vimentin-positive cells were counted in five random (× 40 magnification) fields per lung. Staining was scored on the basis of intensity scale in which + represents low/medium staining and ++ high intensity.

Cell immunofluorescence microscopy

To stain AMs grown in culture, cells were grown on coverslips and fixed in fixation buffer (4% paraformaldehyde/2% sucrose/PBS) for 20 min at room temperature as previously reported (31). Coverslips were then rinsed twice in PBS and permeabilized in permeabilization buffer (0.4% Triton-X and 1% BSA in PBS) for 20 min. Primary antibodies B-Catenin (Santa Cruz) and Stat3 (Cell Signaling) were applied at 1:250 dilution in staining buffer (0.1% Triton-X and 0.1% BSA in PBS) overnight at 4°C in a humid chamber. Coverslips were washed 5 times (5 min each) in wash buffer (0.2% Triton-X and 0.2% BSA in PBS). Secondary antibodies (AlexaFluor secondary 488 or 594, Invitrogen) were applied at 1:250 dilution in staining buffer for 2–3 hours at room temperature in a humid chamber in the dark. Prior to mounting with Vectorshield with DAPI (Vector Laboratories, CA), coverslips were washed two more times in wash buffer. Immunofluorescent analysis was conducted on an Olympus TH4–100 fluorescent microscope using Slidebook V.4.1 digital microscopy.

Quantification of lung tumors

Fixed and embedded lung tissues were sliced into 5-μm sections to obtain five serial sections per lung. Sections were stained with H&E and the number and size of nodules were determined using a histology microscope. Tumor size (area of nodules) was calculated using the measurement tool provided with cellSens v3.2 imaging software (Olympus America).

Culture of primary AMs

Lung tissue was digested as described above to obtain a single-cell suspension. SiglecF$^+$ cells were isolated using anti-SiglecF microbeads (Miltenyi Biotec) and plated in non-treated 6-well plates in RPMI 1640 media containing 1x GlutaMAX, 1x pyruvate, 1x penicillin/streptomycin, 10% fetal bovine serum (FBS), and 20 ng/ml recombinant GM-CSF (Biolegend), as previously described (31). Culture medium was replaced after 16 h of incubation at 37°C and again every 2 days in culture. Cells were collected on days 1 or 6 after plating. Where indicated, AMs were treated overnight with 5 μM of the Wnt/β-catenin inhibitor XAV939 (Sigma) or 1 μM of the Stat3 inhibitor Napabucasin (Fisher Scientific) before cells were harvested.

Western blotting

As previously reported (31), cells were washed once with PBS at room temperature and resuspended in RIPA buffer (PBS containing 1% NP-40, 1% sodium deoxycholate, 1% SDS, 1 mM EDTA, and phosphatase and protease inhibitors). Tissue samples were homogenized directly in RIPA buffer. Lysates were centrifuged and supernatants were removed and subjected to SDS-PAGE. Proteins were transferred to nitrocellulose membranes (Osmonics), and membranes were blocked with 5% milk in PBS incubated with appropriate primary antibodies, and then incubated with Alexa Fluor-conjugated or horseradish peroxidase-conjugated secondary antibodies. Blots were imaged using an Odyssey detection system (Amersham Bioscience) or a ChemiDoc MP imaging system (Bio-Rad).

RNA extraction and qRT-PCR analysis

RNA preparation and RT-PCR analyses were performed as previously reported (31). Briefly, total RNA was extracted from tissues or cells using TRIzol (Ambion) and treated with DNase I. cDNA was synthesized using oligo-dT and random hexamer primers, according to the SYBR Green qPCR protocol (Life Technologies). Total RNA was reverse transcribed using High-Capacity Reverse Transcriptase kits (Invitrogen), according to the manufacturer's protocol. RNA purity and concentration were checked and quantified by reading absorbance at 260 nm and 280 nm in a NanoDrop spectrophotometer (Thermo Fisher). qRT-PCR analysis was performed using SYBR Green RT-PCR kits (Invitrogen) on a Bio-Rad CFX Connect Real-Time System or a Roche LightCycler. *GAPDH* or 18S RNAs served as internal controls. PCR primers were designed using Primer3 and their specificities were checked using BLAST. PCR products were limited to 100–200 bp. Primer sequences are listed in Supplemental Table 4.

RNA-seq analysis

Lung tissues were digested as described above and previously reported (31). F4/80$^+$ CD11c$^+$ SiglecF$^+$ cells were purified by flow cytometry and sorted cells were then processed for gene expression analysis. PolyA RNA was isolated using the NEBNext® Poly(A) mRNA Magnetic Isolation Module, and bar-coded libraries were constructed using the NEBNext® Ultra™ Directional RNA Library Prep Kit for Illumina® (NEB). Libraries were pooled and sequenced from a single end (1×75) using an Illumina NextSeq 500 system with the High Output V2 kit (Illumina). RNA-seq samples were sequenced at a depth of 11–16 million reads.

Illumina Truseq adapters and polyA/polyT sequences were trimmed from raw reads using Cutadapt v2.3 (33), and trimmed reads were aligned to mouse genome version mm10 and Ensembl gene annotations v84 using STAR version 2.7.0d_0221(34), adopting alignment parameters from the ENCODE long RNA-seq pipeline (https://github.com/ENCODE-DCC/long-rna-seq-pipeline). RSEM v1.3.1 was used to obtain gene level estimated counts and transcripts per million (35). FastQC v0.11.5 (https://www.bioinformatics.babraham.ac.uk/projects/fastqc/) and MultiQC v1.8 (36) were used to assess quality of trimmed raw reads and alignment to the genome and transcriptome. To remove poorly expressed genes from downstream analysis, only genes with RSEM estimated counts 5 times the total number of samples were retained for differential expression analysis. Differential expression comparisons were performed using the Wald test implemented in DESeq2 v1.22.2 (37). Genes with a Benjamini–Hochberg-corrected p value of < 0.05 and fold-change of 1.5 or −1.5 were defined as differentially-expressed. Pathway analysis was performed using Ingenuity Pathway Analysis software (Qiagen).

Single-cell library preparation and sequencing

Mice were sacrificed 7 weeks after the first urethane treatment. Lungs were digested as described above and single-cell suspensions were washed with 4% FBS in PBS and incubated 20 min at 5×10^7 cells/ml on ice with 500 ng/ml Fc block (2.4G2, BD Pharmingen). Cells were then incubated 1 h on ice with AF700-conjugated anti-CD45.2 mAb (104, BioLegend). For scRNA-seq libraries, live (DAPI-negative) CD45$^+$ cells were

sorted using a flow cytometer and resuspended in RPMI 1640 medium for counting. Libraries were prepared using Single Cell 3′ Reagent Kits v3.1, Chromium™ Single Cell 3′ Library & Gel Bead Kit v3.1 (10X Genomics, PN-1000196 and PN-1000129) according to the Single Cell 3′ Reagent Kits v3 (PN-1000269) User Guide (Manual CG000315 Rev C). Libraries were sequenced on a NovaSeq S4 system, using half-full lanes for 2 samples, with a mean read depth of 87,000–128,000 reads per cell.

scRNA-seq data pre-processing

The 10X Genomics Cell Ranger pipeline v6.1.2 was used to process scRNA-seq datasets. Single-cell gene counts for each sample were generated using *cellranger count* and mouse genome version mm10 annotated with mouse GENCODE version M28 (38). We obtained a total of 8522 *Siah* WT cells (128,000 mean reads per cell, median of 2674 genes detected per cell) and 6479 *Siah2*$^{-/-}$ cells (103,000 mean reads per cell, median of 2502 genes detected per cell). Gene count matrices for *Siah* WT and *Siah2*$^{-/-}$ cells were aggregated and normalized for effective sequencing depth using *cellranger aggr* applying the "--normalize=mapped" parameter.

Integrated analysis of scRNA-seq datasets

Aggregated gene count matrices for *Siah* WT and *Siah2*$^{-/-}$ scRNA-seq samples were processed using Seurat v4.0.5 (39) and R v4.0.2. The 10X Genomics *cellranger aggr* matrix was converted to Seurat object by retaining genes expressed in ≥10 cells and cells expressing ≥200 genes. Only cells expressing <10% mitochondrial genes and <5000 total genes were retained to remove dead/low quality cells and potential doublets/multiplets, respectively. Integration of *Siah* WT and *Siah2*$^{-/-}$ samples was performed using the *sctransform* normalization method (https://satijalab.org/seurat/articles/integration_introduction.html#performing-integration-on-datasets-normalized-with-sctransform-1). A total of 3000 differentially expressed genes was used in the *SelectIntegrationFeatures* step. The two datasets were integrated using *FindIntegrationAnchors(normalization.method)* and *IntegrateData(normalization.method)*. PCA components were computed using *RunPCA*. Cell clusters were computed using *RunUMAP(dims=1:30)*, *FindNeighbors*, and *FindClusters(resolution=0.5)*, resulting in 17 cell clusters. To visualize gene expression and differential expression analysis, the default assay was set to *"RNA"* and gene counts normalized using *NormalizaData*. Cluster markers were found using *FindAllMarkers*. Differential expression analysis comparisons were performed using *FindMarkers(test.use="MAST")*. Plots were prepared using Seurat and ggplot2 (39,40). Pathway analyses were performed using Ingenuity Pathway Analysis software. RNA-seq and scRNA-seq plots were prepared using ggplot2, ComplexHeatmap and Seurat (39–41). Re-clustering of myeloid clusters (clusters 2, 3, 5) was performed by selecting cells from these clusters and repeating the above-described method. For re-clustering, the 638 most variably expressed genes, rather than the 3000 genes used for integration described above, were selected by retaining genes with a normalized expression variance of >0.4.

Integrated analysis of scRNA-seq data

Raw count (UMI), cell annotation, and sample information were obtained from the Gene Expression Omnibus record (GSE131907; 42). Raw single-cell data was converted to Seurat object using *CreateSeuratObject*. We kept the "Alveolar Mac", "mo-Mac", and "Monocyte" cell types for normal (nLung, 15,338 cells) and tumor (tLung, 6641 cells) patient samples, which corresponded to 22 lung samples from 12 unique patients. Raw UMI counts were normalized using *NormalizeData*, and the 571 most variably expressed genes were selected by retaining genes with a normalized expression variance >0.4. Data were scaled using *ScaleData* and linear dimension reduction was performed using *RunPCA*. Harmony (43) was used for integration of patient data using *RunHarmony*. Cell clusters were computed using *RunUMAP(reduction="harmony", dims=1:30)*, *FindNeighbors(reduction="harmony", dims=1:30)*, and *FindClusters(resolution=0.5)*, resulting in 10 cell clusters. Cluster markers were identified using *FindAllMarkers*. Differential expression analysis was performed using *FindMarkers(test.use="MAST")*. The average expression of 169 upregulated genes in the macrophage pro-fibrotic gene signature (Supplemental Table 3) was computed using *AddModuleScore*.

LUAD analysis

RNA-seq and clinical data from TCGA-LUAD Pan-Cancer 2018 (44) were downloaded from cBioPortal. Survival analysis was performed in R v4.2.1 using a survival algorithm (45). The survival analysis was enabled using survminer, an R. R package version 3.3–1, https://CRAN.R-project.org/package=survival.) (46) and survival Curves were drawn using 'ggplot2'. R package version 0.4.9 (http://www.sthda.com/english/wiki/survminer-r-package-survival-data-analysis-and-visualization), and maxstat (Maximally Selected Rank Statistics) package version 0.7–25 (https://cran.r-project.org/web/packages/maxstat/index.html) (47). Categorization of TCGA-LUAD samples as 'high' and 'low' gene expressors in the TCGA dataset was determined using surv_cutpoint and surv_categorize functions from the survminer package. Survival analyses using gene signatures (multiple genes) were performed by computing the mean expression of the gene signature. Hazard ratios in TCGA-LUAD for each gene were computed in R with the coxph function using the same 'high' and 'low' gene expression categorizations described above. CODEFACS (COnfident DEconvolution For All Cell Subsets) was developed (48) as a tool for deconvoluting cell type-specific gene expression for each sample from bulk expression data given either precomputed estimates of cell abundance or a cell type-specific signature.

Statistical analysis

At least 3 samples were used in each experimental group. All experiments were performed at least three times to establish statistical power and reproducibility. Prism v7 software (GraphPad) was used for statistical analysis. Differences between two groups were assessed using a two-tailed unpaired *t*-test. Survival analysis was performed using the Kaplan–Meier method, and survival and hazard ratio p values were computed using the log-rank test. Differences in cell-type compositions between TCGA-LUAD patients were assessed using Wilcoxon's rank sum test.

Data Availability

The data analyzed in this study were obtained from Gene Expression Omnibus (GEO) at GSE13190. Raw and processed RNA sequencing data have been deposited at Gene Expression Ominibus GEO under accession GSE215993 (GSE215920 bulk RNA-seq, GSE215992 scRNA-seq). Raw data generated in this study were generated by performing immunohistochemistry, Western blots and qPCR analyses, all are available upon request from the corresponding author.

Results

Siah1a and Siah2 are required for AM terminal differentiation and maturation.

To establish mice with conditional loss of both *Siah1a* and *Siah2* (*Siah1a/2*) in myeloid cells, we generated *Siah1a$^{f/f}$::Siah2$^{f/f}$* mice and crossed them with myeloid-specific Cre (*Lyz2^{Cre}*) mice to ablate *Siah1a/2* (*Siah1a/2$^{f/f}$::Lyz2^{Cre}*; hereafter referred to as *Siah1a/2^{L-KO}*). Total macrophage (CD45$^+$ CD11b$^+$ F4/80$^+$) frequency in spleen, heart, kidney, and lungs of *Siah1a/2^{L-KO}* and WT mice was similar (Fig. 1A and Supplemental Fig. S1A). We next used markers of macrophage subtypes to further characterize lung macrophages into AMs (CD11b^{low} F4/80$^+$), IMs (CD11b$^+$ F4/80$^+$), and additional subpopulations by flow cytometry (FACS). Frequency of CD45$^+$ cells (Supplemental Fig. S1B) and total IMs (Fig. 1A) was comparable in lungs of WT and *Siah1a/2^{L-KO}* mice. In striking contrast, frequencies of both total (CD11b^{low} F4/80$^+$; Figs. 1B, 1F) and mature (CD11b^{low} F4/80$^+$ CD11c$^+$ SiglecF$^+$; Figs. 1C, 1D, 1F) AMs were significantly reduced in lungs of *Siah1a/2^{L-KO}* relative to WT mice, and conversely, frequency of immature AMs (CD11b^{low} F4/80$^+$ CD11c$^+$ SiglecF^{low}) significantly increased in *Siah1a/2^{L-KO}* lungs (Figs. 1E, 1F). These findings suggest overall that AMs require *Siah1a/2* for differentiation and maturation. Of note, most CD11b^{low} F4/80$^+$ macrophages in both WT and *Siah1a/2^{L-KO}* lungs were positive for the mannose receptor CD206 (Supplemental Fig. S1C).

In addition to frequency of macrophage subsets, we also examined absolute expression levels of markers by FACS (reported as mean fluorescence intensity [MFI]). Notably, expression levels of CD11c and SiglecF were significantly lower, while expression of CD11b was significantly higher on mature AMs from *Siah1a/2^{L-KO}* mice (Fig. 1G), confirming that *Siah1a/2*-deficient AMs exhibit a more immature-like phenotype relative to WT mice. As F4/80, MHCI, CD80, and CD206 expression was comparable on mature AMs from both genotypes (Supplemental Fig. S1D), differences in CD11c and SiglecF levels likely reflect defects in macrophage differentiation induced by *Siah1a/2* loss.

Macrophages can present significant differences between gender (49). To determine if the phenotypes we observed were gender-dependent, we performed FACS analysis of AMs prepared from lungs of *Siah1a/2^{L-KO}* or WT male and female mice. *Siah1a/2^{L-KO}* mice of both genders exhibited a reduced frequency of total AMs and mature AMs relative to WT mice (Supplemental Fig. S1E). Moreover, the frequency of immature AMs was higher in lungs of *Siah1a/2^{L-KO}* relative to WT mice, whereas SiglecF expression in AMs from *Siah1a/2^{L-KO}* mouse lung was significantly lower relative to WT, in both male and

female mice (Supplemental Fig. S1E–F). These observations suggest that the AM phenotype observed in macrophages upon Siah1a/2 ablation occurs independent of gender.

Because a subpopulation of lung IMs reportedly expresses CD11c (50), which is downregulated on mature AMs following *Siah1a/2* deletion, we asked whether either abundance of CD11c$^+$ IMs or CD11c expression levels on IMs was altered by *Siah1a/2* deletion. We observed a small but significant decrease (from 43% to 33%) in CD11c$^+$ IM frequency in lungs of *Siah1a/2*$^{\text{L-KO}}$ relative to WT mice, concomitant with a significant increase in CD11c$^-$ IMs (Fig. 1H), although levels of CD11c protein were comparable between genotypes (Supplemental Fig. S1G). We also observed a significant decrease in NK1.1$^+$ cell frequency, but not that of other immune cell populations (CD4$^+$ T cells, CD8$^+$ T cells, B cells or monocytes) in *Siah1a/2*$^{\text{L-KO}}$ relative to WT lungs (Supplemental Fig. S1H). Overall, these data suggest that Siah1a and/or Siah2 are required for AM differentiation to a fully mature state, and that both had limited effect on CD11c$^+$ IM infiltration to the lung.

To assess individual contributions of *Siah1a* and *Siah2* to AM differentiation, we generated mice with macrophage-specific deletion of *Siah1a* (*Siah1a*$^{\text{L-KO}}$) or *Siah2* (*Siah2*$^{\text{L-KO}}$) alone and compared mature AM populations in lung with those seen in either WT or double-mutant *Siah1a/2*$^{\text{L-KO}}$ mice. Frequency of mature AMs was comparable in WT, *Siah1a*$^{\text{L-KO}}$, and *Siah2*$^{\text{L-KO}}$ lungs (Figs. 1I and 1J). We detected a small but significant decrease in CD11c and SiglecF MFI on *Siah1a*$^{\text{L-KO}}$ mature AMs and a small but significant increase in SiglecF MFI on *Siah2*$^{\text{L-KO}}$ compared with WT AMs (Figs. 1I and 1J). Frequency of total lung IMs (CD11b$^+$ F4/80$^+$) was not altered by *Siah1a* KO, while *Siah2* KO resulted in a small but significant decrease. Conversely, respective frequencies of CD11c$^+$ and CD11c$^-$ IMs significantly increased and decreased following deletion of *Siah1a*, but not *Siah2* (Supplemental Fig. S1I). Taken together, these data indicate that both Siah1a and Siah2 are necessary for AM maturation.

Because *Lyz2* Cre is expressed embryonically (13,16) and Lyz2 is also expressed in neutrophils, we next asked whether Siah1a/2 were required for AM differentiation and maturation during embryonic development and whether *Siah1a/2* function in AMs was cell-intrinsic. To this end, we performed comparable analyses of lungs of mice in which *Siah1a* and/or *Siah2* ablation is driven by *Cd11c*$^{\text{Cre}}$ (referred to as $^{\text{C-KO}}$ mice), which is most highly expressed in AMs postnatally and is not expressed by neutrophils (13,16). As seen in lungs of *Lyz2*$^{\text{Cre}}$ mice, frequencies of total lung CD45$^+$ cells were comparable in WT, *Siah1a*$^{\text{C-KO}}$, *Siah2*$^{\text{C-KO}}$, and *Siah1a/2*$^{\text{C-KO}}$ mice (Supplemental Fig. S1J). Moreover, similar to *Siah1a/2*$^{\text{L-KO}}$ phenotypes, frequency of mature AMs and CD11c$^+$ IMs decreased and that of CD11c$^-$ IMs increased in *Siah1a/2*$^{\text{C-KO}}$ relative to WT mice (Figs. 1K, 1M). AMs from *Siah1a/2*$^{\text{C-KO}}$ mice expressed lower levels of CD11c and SiglecF compared with cells from WT mice (Fig. 1L), as seen in analysis using the Lyz2 driver. Of interest, single-KO of either *Siah1a* or *Siah2* did not alter frequency of mature AMs, CD11c$^+$ IMs, or CD11c$^-$ IMs in lungs as compared with WT mice (Figs. 1K, 1M). Within the mature AM population, CD11c expression levels were comparable in WT, *Siah1a*$^{\text{C-KO}}$, and *Siah2*$^{\text{C-KO}}$ cells, whereas only *Siah1a* deletion promoted a small but significant decrease in SiglecF expression (Fig. 1L). Consistent with observations in *Siah1a/2*$^{\text{L-KO}}$ *mice*, single- and double-*Siah1a/2*$^{\text{C-KO}}$· had no effect on frequency of DCs or other immune cell populations in lung (Supplemental

Fig. S1K), except for NK1.1$^+$ cells, whose frequency markedly decreased in *Siah1a/2*$^{C-KO}$ relative to WT mice (Supplemental Figs. S1 L). These observations suggest that Siah1a and Siah2 expression in the myeloid population underlies NK1.1$^+$ cell recruitment to lungs. Collectively, data derived from *Siah1a/Siah2*$^{C-KO}$ mouse models confirm findings obtained seen using the *Lyz2* driver and suggest a cell-intrinsic function for Siah1a/2 in AMs maturation and differentiation.

Siah1a and Siah2 regulate maturation of fetal monocytes to AMs.

To assess a potential Siah1a/2 function in the transition from fetal to mature AMs, we assessed frequency of immature AMs in E17.5 WT and *Siah1a/2*-deficient mouse embryos. We observed that the frequency of immature fetal AMs (F4/80^{int} CD11c^{int}) was comparable in embryos of both genotypes (Fig. 2A). While CD11b or F4/80 MFI was similar in both genotypes, the CD11c MFI markedly decreased in *Siah1a/2*$^{L-KO}$ versus WT AMs at E17.5, suggesting a delay in differentiation (Fig. 2B). At birth (postnatal day 0, P0), frequency of total AMs (CD11b^{low} F4/80$^+$) was comparable in lungs of *Siah1a/2*$^{C-KO}$ and WT mice (Fig. 2C), while the frequency of mature AMs decreased (Figs. 2C, D). *Siah1a/2* deletion also significantly decreased the MFI of CD11c, SiglecF, and, to a lesser extent, F4/80 on mature AMs (Figs. 2E, 2D). Although lung IM frequency was comparable between genotypes, frequencies of CD11c$^-$ and CD11c$^+$ IMs increased and decreased at E17.5, respectively, following macrophage-specific *Siah1a/2* deletion (Fig. 2F). These data strongly suggest that *Siah1a/Siah2* deletion suppresses AM maturation but not development of immature AMs in fetal lung.

Siah1a and Siah2 are required for AM regeneration in the bone marrow.

As noted, AMs self-renew and proliferate under normal physiological conditions but can be replenished from BM-derived monocytes under inflammatory conditions or after bone marrow transplant (50). To determine whether Siah1a/2 are required for AM reconstitution from the BM, we established a BM chimeric mouse model in which BM cells from CD45.2$^+$ WT or CD45.2$^+$ *Siah1a/2*$^{L-KO}$ mice were co-injected with an equal number of CD45.1$^+$ BM cells into irradiated C57BL/6J recipient mice, which were then assessed for AM reconstitution in lung by FACS 8 weeks later. The frequency of CD45.2$^+$ mature AMs was approximately 70% in mice reconstituted with CD45.2$^+$ WT BM but only 50% in mice reconstituted with *Siah1a/2*$^{L-KO}$ BM (Fig. 3A, 3B). Also, levels of CD11c and SiglecF expression were markedly lower, while F4/80 expression was unchanged, on CD45.2$^+$ mature AMs from mice reconstituted with *Siah1a/2*$^{L-KO}$ relative to WT BM (Fig. 3C), suggesting overall that AM repopulation and maturation are impaired by *Siah1a/2* loss. Frequency of CD11c$^+$ IMs was also lower in mice reconstituted with *Siah1a/2*$^{L-KO}$ (~30%) compared to WT (~37%) BM (Fig. 3D), whereas reconstitution of CD11c$^-$ IMs and other immune cells was unaffected (Fig. 3E).

Results reported above suggest that *Siah1a/2* loss primarily affects regeneration of AMs and CD11c$^+$ IMs from BM. To confirm this, we repeated the mixed BM experiments using *Cd11c*^{Cre} mice. As seen in *Lyz2*^{Cre} mice, ~70% and 30% of mature AMs were reconstituted by transfer of WT and *Siah1a/2*$^{C-KO}$ BM, respectively (Supplemental Fig. S2A). Similarly, CD11c expression was significantly lower on AMs derived from *Siah1a/2*$^{C-KO}$ relative to

WT BM (Supplemental Fig. S2B), but we observed no differences in frequencies of CD11c$^+$ or CD11c$^-$ IMs (Supplemental Fig. S2C). These data confirm the importance of Siah1a and Siah2 expression in maturation of AMs from BM-derived monocytes.

Siah1a/2 controls the physiological immunoregulatory function of AMs.

Given that AM maturation requires *Siah1a/2*, we next asked what genes/pathways underlie this activity using RNA-seq analysis of sorted AMs (CD11c$^+$ F4/80$^+$ SiglecF$^+$) from lungs of WT, *Siah1a/2*$^{L-KO}$, and *Siah1a/2*$^{C-KO}$ mice. Principal component analysis (PCA) showed similar patterns of gene expression in cells from both KO genotypes and a clear segregation between WT and *Siah1a/2*^{KO} cells along the main component PC1 (Fig. 4A). Analysis of genes differentially expressed (DEGs) in *Siah1a/2*$^{L-KO}$ and *Siah1a/2*$^{C-KO}$ relative to WT AMs revealed similar patterns of gene expression in AMs from both KO genotypes (Supplemental Fig. S2D). In total, 565 upregulated and 363 downregulated DEGs were identified in AMs from *Siah1a/2*$^{L-KO}$ relative to WT mice (Fig. 4B, Supplemental Fig. S2D). Given that AMs from *Siah1a/2*$^{L-KO}$ mice exhibit predominantly immature phenotypes and that GM-CSF/PPARγ signaling is implicated in AM differentiation and maturation, we searched for changes in these pathways among DEGs. Although we observed a small but significant increase in *Csf2rb* and *Tgfbr2* mRNA levels in *Siah1a/2*$^{L-KO}$ relative to WT AMs, expression of all other GM-CSF/PPARγ pathway components were comparable in both genotypes (Supplemental Fig. S2E). Likewise, immunofluorescence staining for PPARγ in primary lung AMs cultured 1 day in GM-CSF showed a similar degree of PPARγ nuclear localization in cells of both genotypes (Supplemental Fig. S2F), suggesting that *Siah1a/2* loss likely does not alter GM-CSF/PPARγ signaling during AM maturation.

To identify pathways dysregulated by *Siah1a/2* loss, we performed Ingenuity Pathway Analysis (IPA) of DEGs identified in AMs. Among signaling pathways most activated by *Siah1a/2* loss were STAT3, TGFβ, the acute phase response, and actin cytoskeleton signaling (Fig. 4C). Accordingly, the gene signature of *Siah1a/2*$^{L-KO}$ AMs was markedly pro-inflammatory (Fig. 4D). Of note, most components of the inflammatory signature seen in AMs (such as Serpine1, Arg1, Chil3 and S100A8; Fig. 4D, highlighted in red; Supplemental Table 1) have been observed in bleomycin-treated mice, which exhibit lung fibrosis (51) associated with increased Stat3 and b-catenin activity in AMs (52). Indeed, AMs derived from lungs of patients with pulmonary fibrosis exhibit a Stat3 activation signature (53). Interestingly, conditional β-catenin ablation in macrophages alleviates bleomycin-induced fibrosis in mice (54), while β-catenin activation is associated with increased inflammation (55) and GADD45G expression, the latter implicated in slowing cell proliferation (56). We also identified DEGs functioning in proliferation in RNA-seq analysis of our genetic *Siah1a/2*$^{L-KO}$ mouse derived lung samples (Fig. 4E), consistent with the reduction in mature AM frequency seen in *Siah1a/2*$^{L-KO}$ and *Siah1a/2*$^{C-KO}$ relative to WT mice (Figs. 1C, K). Finally, we confirmed downregulation of Siah1 and Siah2 mRNA levels (Supplemental Fig. S2G) and altered expression of genes involved in proliferation in primary AMs isolated from *Siah1a/2*$^{L-KO}$ relative to WT mice (Fig. 4G, Supplemental Fig. S2H).

RNA-seq analysis also revealed increased expression of β-catenin and Stat3 targets within the inflammatory signature of AMs from *Siah1a/2*[L-KO] versus WT mice (Fig. 4D). Indeed, *Siah1a/2*-deficient AMs exhibited increased levels of β-catenin transcripts (Fig. 4D) and increased nuclear localization of β-catenin protein, the latter indicative of activation (Fig. 4F). Analysis of cultured primary *Siah1a/2*[L-KO] AMs confirmed markedly increased expression of the β-catenin targets Serpine1, Gadd45g and Axin2, an increase blocked by treatment with the β-catenin inhibitor XAV939 (Fig. 4G). Likewise, induction of Stat3 target genes (such as Marco and S100A8) seen in *Siah1a/2*[L-KO] AMs was antagonized by treatment with the Stat3 inhibitor Napabucasin (Fig. 4H). Treatment with either XAV939 or Napabucasin blocked increases in expression of the inflammatory marker Chil3 (Fig. 4I), suggesting that both Stat3 and β-catenin contribute to inflammatory phenotypes. Increase in metabolic signaling associated with increased β-catenin activation was also seen in *Siah1a/2*[KO] AMs (Supplemental Fig. S2I). Together, these data indicate that phenotypes observed upon *Siah1a/2* deletion in AMs can be linked to pro-inflammatory and pro-fibrotic gene signatures, which are associated with elevated β-catenin and Stat3 signaling (Fig. 4D).

Macrophage-specific *Siah1a/2* deletion exacerbates urethane-induced lung cancer.

Given AM abundance in lung in physiological conditions, we asked whether Siah1a/2 loss in AMs would alter lung cancer development and/or progression. To do so, we injected WT or *Siah1a/2*[L-KO] mice weekly for 6 weeks with urethane, a carcinogen that induces KRAS mutation and promotes lung cancer development (57). Lungs of *Siah1a/2*[L-KO] mice, collected 24 weeks after the first urethane injection, harbored a greater number of tumor nodules over a larger area than did lungs of urethane-treated WT mice (Figs. 5A–5C). Immunohistochemical analysis revealed a significant increase in the number of Ki67-positive cells in lung lesions of *Siah1a/2*[L-KO] relative to WT mice, suggestive of increased cancer cell proliferation (Supplemental Fig. S3A). Immunohistochemical analysis of AMs (CD11c+ round-shaped cells) confirmed AM infiltration in lesions of both WT and *Siah1a/2*[L-KO] lungs (Supplemental Fig. S3B–C). Of interest, AM infiltration was observed both in areas of epithelial hyperplasia (Supplemental Fig. S3B) and in adenomas (Supplemental Fig. S3C): in both cases AMs appeared to be in close contact with epithelial cells, suggesting cell-cell communication via either secreted factors, membrane receptors or channels. The frequency of mature AMs in lungs of tumor-bearing WT mice was lower than frequencies seen in normal WT mice (12% *vs* 22% of CD45+ lung cells, Figs. 5D *vs* Fig. 1C), and even fewer AMs were detected in lungs of tumor-bearing *Siah1a/2*[L-KO] mice (4% of CD45+ lung cells, Fig. 5D). In contrast, there were no changes in the number of total lung CD45+ cells in lungs of tumor-bearing WT and *Siah1a/2*[L-KO] mice (Supplemental Fig. S4A).

Of note, while immature AMs were virtually undetectable in lungs of normal WT mice (Figs. 1E, 1F), their abundance increased in WT mice after urethane treatment and even more so in urethane-treated *Siah1a/2*[L-KO] mice (Figs. 5E, 5F). In the mature AM population of *Siah1a/2*[L-KO] mice, urethane administration significantly decreased expression levels of CD11c, SiglecF and the costimulatory protein CD80 as compared with mature AMs seen in urethane-treated WT mice (Fig. 5G). In contrast, while CD11c− IM frequency slightly increased in tumor-bearing *Siah1a/2*[L-KO] mice, we noted a significant decrease in CD11C+ cells relative to those seen in WT mice (Figs. 5H, 5I). Expression of MHCI, CD206,

CD11c, and CD80 was comparable in lung CD11c^{+} IMs from *Siah1a/2*[L-KO] and WT mice (Supplemental Fig. S4B), suggesting that both genotypes exhibit a comparable degree of activation despite the lower frequency of CD11c^{+} IMs seen upon Siah1a/2 depletion. Frequencies of B, CD4^{+} T, and CD8^{+} T cells in lungs of WT and *Siah1a/2*[L-KO] mice were also comparable, but frequencies of CD8^{+} CD44^{+} T cells and activated (B220^{+}) NK1.1^{+} cells decreased following *Siah1a/2* loss (Supplemental Fig. S4C). Together, these data suggest that the presence of macrophages lacking *Siah1a/2* enhances tumor cell proliferation and suppresses T and NK cell activity, allowing tumors to escape an immune response and favoring their progression.

Siah1a/2 deletion in macrophages promotes a pro-fibrotic phenotype.

To identify signaling pathways potentially altered in immune cells by *Siah1a/2* deletion in lung macrophages, we performed scRNA-seq of CD45^{+} cells sorted from lungs of WT or *Siah1a/2*[L-KO] mice, 1 week after the final urethane treatment. scRNA-seq analysis of WT (n=7884) and *Siah1a/2*[L-KO] (n=6035) CD45^{+} cells identified 17 immune cell clusters with distinct gene expression patterns (Figs. 6A, 6B), including NKs (clusters 1 and 13), neutrophils (cluster 12), B cells (cluster 15), T cells (clusters 0, 4, 6, 7, 8, 10), myeloid cells (clusters 2, 3, 5 and 11), plasmacytoid DCs (cluster 9), conventional DCs (cluster 16), and basophils (cluster 14). T cell populations were distributed into terminally exhausted effector (cluster 0), effector (cluster 6), and proliferating effector (cluster 10) CD8^{+} cells, effector (cluster 7) and Treg (cluster 4) CD4^{+} cells, and CD4^{−} and CD8^{−} CD3^{+} cells (cluster 8) (Figs. 6A, 6B).

Siah1a/2 deletion in macrophages markedly changed frequencies of immune cells in lung relative to WT mice, including increases in neutrophils (cluster 12; 2.45% *vs* 1.15%) and decreases in CD8^{+} effector/proliferative cells (cluster 10; 2.93% *vs* 4.46%) (Supplemental Fig. S5A). Within the myeloid population of Csf1r^{+} cells (clusters 2, 3, and 5), cluster 2 was enriched for AM markers (Apoe, Mrc1/CD206, Cd72, and Itgax; Fig. 6B). Cluster 2 was also positive for genes indicative of monocytic origin (Ly6c2, Fcgr1 and H2-a) and may represent a mix of resident AMs (mature and immature-like) and AMs of monocytic origin (Fig. 6B). Analysis of gene expression (Fig. 6B) mapped monocytes to cluster 3 (Ly6c-expressing) and macrophages to cluster 5 (Hp, Ear2, Ace, Chil3 and Fn1).

IPA analysis identified upregulation of genes associated with fibrosis and tumor progression within AMs of *Siah1a/2*[L-KO] macrophage cluster 2 (Fig. 6C). Accordingly, in pathologic states, AMs showing an immature-like state reportedly exhibit a unique inflammatory signature similar to that seen in fibrotic macrophages (51).

Increased expression of glycolytic genes, which is linked with a pro-fibrotic phenotype (58), within cluster 2 was also consistent with increased macrophage activity (Fig. 6D). Additional differences identified by IPA between macrophages of both genotypes included increased mitochondrial respiration (cluster 5; Supplemental Fig. S5B). Macrophages possessing an immature-like phenotype were enriched upon *Siah1a/2* ablation in cluster 2, as reflected by increased Itgam (CD11b) expression concomitant with decreased Itgax (CD11c) and Cx3cr1 expression (Fig. 6E). Similar to AMs from cluster 2, *Siah1/2*-deleted monocytes (cluster 3) exhibited increased expression of genes associated with fibrosis (Fig.

6F). Consistent with inflammatory and fibrotic phenotypes, *Siah1a/2*-deficient AMs isolated from lungs of urethane-treated mice exhibited increased nuclear localization of β-catenin and Stat3, which is linked to both inflammation and fibrosis, indicative of activation (Supplemental Fig. S5C and D).

Among transcripts upregulated in *Siah1a/2*[L-KO] AM cluster 2 were Plaur, Lgals3, Ccl9 and Cebpb (Fig. 6C), all implicated in immunosuppression. Of interest, Lgals3 reportedly suppresses T and NK cell immune function (59) and promotes tumor growth (60), consistent with phenotypes observed in our mouse model (Supplemental Fig. S3A and S4C). Correspondingly, immunofluorescence analysis confirmed increased Galectin3 (Lgals3) protein levels in AMs (CD11c^{+} round-shaped cells) derived from *Siah1a/2*[L-KO] relative to WT lung lesions (Supplemental Fig. S6A). Increased protein levels of Vimentin, whose expression is upregulated in cluster 2 macrophages (Fig. 6C), were confirmed by immunofluorescence of AMs (CD206^{+} round-shaped cells) from *Siah1a/2*[L-KO] as compared to WT lungs (Supplemental Fig. S6B). Of note, CD206/CD11c colocalization was seen in round-shaped cells from both *Siah1a/2*[L-KO] and WT lungs (Supplemental Fig. S6C), consistent with our observations in FACS analysis (Supplemental Fig. S1C). These data suggest that *Siah1a/2*[L-KO] macrophages release factors, such as Galectin3, conducive to immunosuppression and tumor proliferation.

Our initial analyses of the three myeloid clusters (2, 3, 5; Fig. 6A) did not separate resident from immature AMs; therefore, we re-clustered these groups and obtained nine myeloid subclusters expressing genes, albeit at different levels, associated with a monocytic origin (Figs. 7A and B). Three subclusters (1, 2, and 3) exhibited characteristics of monocyte populations, and four (5, 6, 7, and 8) consisted of more differentiated resident macrophages (Fig. 7C), of which subclusters 5 and 8 consisted of mature AMs. We also identified a unique group of T cells positive for F4/80 and CD11c (cluster 4; Fig. 7C). Lastly, subcluster 0 expressed AM markers but at a level lower than that seen in mature AMs (clusters 5 and 8), suggesting that cluster 0 contains immature AM (Fig. 7C).

Siah1a/2[L-KO] mice showed a decreased proportion of AMs (subclusters 5 and 8) relative to WT mice (Supplemental Fig. S7A), while immature AMs (subcluster 0) showed increased *Itgam* levels and decreased *Itgax* and *Cxc3r1* levels (Fig. 7D), confirming our FACS and gene expression analyses. Lastly, we observed increased expression of genes implicated in glycolysis (Supplemental Fig. S7B), which is reported in pro-fibrotic AMs (58) and coincides with increased expression of genes associated with fibrosis (Fig. 7E), in *Siah1a/2*-deficient AMs of cluster 0. These data indicate that *Siah1a/2* loss in AMs promotes pro-tumorigenic and pro-fibrotic phenotypes. LY6C protein frequency in AMs, immature AMs and IMs was largely comparable in WT and *Siah1a/2*-ablated cells (Supplemental Fig. S7C). This latter finding excludes the possibility that the immature-like state of *Siah1a/2*-deleted AMs is attributable to dysregulated recruitment of bone marrow-derived monocytes.

To assess the clinical relevance of our findings, we examined expression of genes significantly upregulated (72 genes) in immature AMs of *Siah1a/2*[L-KO] compared to WT mice (Supplemental Table 2) in two TCGA-LUAD patient datasets. Of the 72-gene signature identified in mice, 62 unique genes were mapped in both human datasets, and patients

were then stratified into two groups based on low and high expression of these genes. Survival analysis identified a significant association between high expression of the 62-gene signature and poor prognosis (Fig. 7F), a trend comparable in female and male populations (Supplemental Fig. S7D). Second, prediction of cell abundance based on bulk RNAseq deconvolution (48) of TCGA LUAD patients identified increased infiltration of myeloid cells (CD14$^+$) that exhibited relatively high average expression of the 62-gene signature (Fig. 7G). To determine which of 62 genes is linked with poorer survival in the TCGA-LUAD dataset, we calculated individual hazard ratios for these genes, which identified genes involved in glycolysis, plasmin generation, and extracellular matrix degradation as associated with worse survival (Supplemental Fig. S7E). Notably, the same genes set are expressed in tumor-associated macrophages and are linked to cancer progression (61,62).

We next asked whether the 62-gene signature identified in the cluster of immature-like AMs in lungs of *Siah1a/2*$^{L-KO}$ mice was expressed by macrophages in LUAD tumor tissues. To do so, we performed scRNA-seq data from macrophages and monocytes derived from tumor and non-malignant lung tissues from 12 patients with metastatic LUAD, followed by data re-clustering (42). This analysis identified 10 subclusters (Fig. 8A), of which five (0, 1, 2, 8, and 9) expressed markers specific to human AMs (PPARγ, FABP4, MARCO, MCEMP1, and CXCL16 (63,64), and low levels of the monocytic marker CD14 (Fig. 8B). Subcluster 2 expressed the lowest levels of the 5 AM markers and highest levels of CD14 (Fig. 8B), similar to patterns seen in immature-like AMs of monocytic origin derived from our mouse model (Fig. 7C). Notably, immature AMs (cluster 2) and monocyte-macrophage clusters (3 and 6) showed highest expression of CTSB (in clusters 2 and 3) and TREM2 (in clusters 2 and 6) (Fig. 8B), proteins associated with cancer metastasis and immunosuppression, respectively (65,66). Notably, immature AMs (cluster 2) and monocyte-macrophage clusters (3 and 6) were enriched in lung tumor tissues as compared with normal lung tissue from LUAD patients (Supplemental Fig. S8A and B). We also observed increased expression of the monocytic marker CD14 and decreased expression of AM markers in tumor versus normal tissues (Fig. 8C, Supplemental Fig. S8C). Subclusters 2, 3 and 6 from tumor tissue exhibited highest expression of pro-inflammatory/pro-fibrotic genes (such as CCL2, CCL3, SEPP1, and PLA2G7; Fig. 8C) relative to normal lung tissue, confirming findings in the genetic mouse model. These observations suggest that immature AMs present in LUAD tissue are potentially linked with pro-tumorigenic functions (Fig. 8C, Supplemental Fig. S8C). As confirmation, we compared the 62-gene signature in mouse subcluster 0 with genes expressed in monocytes and macrophages from tumor and normal lung tissue from LUAD patients and observed the greatest enrichment of this gene-set in immature-like AMs from tumor tissues (subcluster 2; Fig. 8D).

Given that TAMs exhibit an immature-like phenotype and a pro-fibrotic signature, we assessed expression of 169 genes upregulated in AMs obtained from patients with pulmonary fibrosis (67) (Supplemental Table 3). We validated a pro-fibrotic signature in monocytes and macrophages from tumor and normal lung tissue of LUAD patients. Indeed immature-like AMs in subcluster 2 and in monocyte/macrophage cluster 3 of human tumor tissue exhibited the most pronounced enrichment of a pro-fibrotic signature (Fig. 8E). These observations provide independent support in patients with LUAD for the enhanced

pro-fibrotic signature seen in immature-like AMs initially identified in our genetic mouse model.

As smoking is associated with an increased risk of lung cancer and mortality (68), we compared expression of the pro-fibrotic gene signature identified in patients with pulmonary fibrosis to gene expression signatures seen in macrophages from normal lung and tumor tissues of LUAD patients who were current, ex-, or never-smokers. We observed strikingly increased expression of the pro-fibrotic signature in macrophages (mostly in subclusters 2 and 3) from lung tumor tissues of current and ex- smokers, relative to never-smokers (Fig. 8F). No differences among current-, ex- and never smokers were detected in expression of the pro-fibrotic signature in myeloid cells obtained from normal lung tissues (Supplemental Fig. S8D). These data overall confirm the relevance of a urethane-induced lung cancer model in *Siah1a/2*^KO mice to human lung cancer and highlight the importance of macrophages in conferring a pro-fibrotic signature, one highly pronounced in smokers and ex-smokers (Fig. 8G).

Discussion

While the function of macrophages in lung inflammation is well known, mechanisms used by these cells to alter lung homeostasis and promote pathological transformation remain poorly understood. Here we demonstrate that macrophage-specific deletion of *Siah1a/2* ubiquitin ligases promotes accumulation of AMs in an immature-like state and induces expression of pro-fibrotic and pro-inflammatory gene signatures. The use of independent but complementary Lyz2^Cre- and Cd11c^Cre-driven genetic models confirmed our principal finding that Siah1a and Siah2 play crucial roles in AM differentiation and maturation and in regulating expression of key gene signatures relevant to pulmonary inflammation, fibrosis, and cancer.

The major effects of macrophage-specific *Siah1a/2* ablation were restricted to AMs, which are the most abundant population of lung macrophage. While AM differentiation is thought to be primarily regulated by GM-CSF/PPARγ and TGFβ signaling (13,16,69), our data revealed that Siah1a/2 contributes to AM maturation independently of the GM-CSF/PPARγ pathway. Siah1a/2 were shown to modulate AM activity *via* activation of Stat3 and β-catenin signaling pathways, conferring a pro-tumorigenic phenotype. Notably, Stat3 plays an important role in the host response to injury and is activated in AMs during lung injury (70), as seen in patients with lung fibrosis (53). While Stat3 was previously reported to bind to Siah proteins (71), the significance of this interaction in the context of inflammation remains unclear. Complementing effects of Stat3 in AMs is β-catenin, a critical factor in cytoskeletal organization and cell migration, which was reported to be a Siah substrate (72). Elevated β-catenin signaling is implicated in differentiation (54) of AMs, and is observed in AMs from lungs treated with bleomycin (53) and in tumor associated macrophages (55). Likewise, mice with macrophage-specific *Siah1a/2* ablation exhibited an immature-like phenotype with pro-inflammatory and -fibrotic signatures associated with elevated Stat3 and β-catenin activity. Indeed, these changes resemble lung fibrosis in humans, a condition associated with increased frequency of immature AMs (51). Previous studies have pointed to the importance of Siah2 in regulating Hippo and HIF pathways (22,73), which are implicated

in macrophage polarization or pro-tumorigenic activities. We confirmed Siah1a/2 control of AM differentiation and inflammatory signaling in a model of urethane-induced pulmonary adenocarcinoma. Notably, lung tumors in these mice were more abundant and larger in *Siah1a/2*$^{L-KO}$ as compared to WT mice, exhibited increased numbers of tumor-associated exhausted T cells, a decreased frequency of activated NK cells, and increased expression of genes implicated in tumor proliferation and immunosuppression.

Tissue-resident AMs self-renew under normal physiological conditions but are replaced by monocyte-derived AMs following infection or injury (12,13). Immature AMs are reportedly enriched in several lung pathologies, including infection and fibrosis (50,51), but not in lung cancer. Here, we demonstrate that, during lung cancer development, the pool of tissue-resident AMs is replaced by monocyte-derived AMs that exhibit immature-like phenotypes and are marked by a pro-fibrotic/pro-inflammatory gene signature, distinct from that seen in resident AMs.

Analyses of myeloid cells from lungs of LUAD patients were consistent with findings in the mouse model and confirmed a link between the pro-fibrotic signature seen in TAMs and smoking. Furthermore, high expression of a 62-gene signature upregulated in *Siah1a/2*^{KO} immature-like AMs was associated with poor survival of LUAD patients. An independent AI-based deconvolution of scRNA-seq datasets from LUAD patients showed that the same gene signature is associated with higher infiltration of CD14$^+$ myeloid cells and worse survival. These independent analyses highlight the importance of monocyte/macrophage infiltration for lung cancer progression.

Overall, this study has uncovered new roles for Siah1a/2 ubiquitin ligases in the differentiation of AMs and revealed how these factors impact lung inflammation, fibrosis, and cancer. Our findings highlight novel mechanisms underlying macrophage regulation in lung cancer and identify a select macrophage population that could be monitored for treatment stratification or targeted as therapy for LUAD.

Supplementary Material

Refer to Web version on PubMed Central for supplementary material.

Acknowledgements

References

1. Jin MZ, Jin WL. The updated landscape of tumor microenvironment and drug repurposing. Signal Transduct Target Ther 2020;5:166 [PubMed: 32843638]

2. Bejarano L, Jordao MJC, Joyce JA. Therapeutic Targeting of the Tumor Microenvironment. Cancer Discov 2021;11:933–59 [PubMed: 33811125]

3. van der Leun AM, Thommen DS, Schumacher TN. CD8(+) T cell states in human cancer: insights from single-cell analysis. Nat Rev Cancer 2020;20:218–32 [PubMed: 32024970]

4. Murphy TL, Murphy KM. Dendritic cells in cancer immunology. Cell Mol Immunol 2022;19:3–13 [PubMed: 34480145]

5. Wu K, Lin K, Li X, Yuan X, Peiqing Xu P, Ni P, Xu D. Redefining Tumor-Associated Macrophage Subpopulations and Functions in the Tumor Microenvironment Front Immunol 2020; 4:11:1731.

6. Pan Y, Yu Y, Wang X, Zhang T. Tumor-Associated Macrophages in Tumor Immunity. Front Immunol 2020; 3:11:583084.

7. Sher T, Dy GK, Adjei AA. Small cell lung cancer. Mayo Clin Proc 2008;83:355–67 [PubMed: 18316005]

8. Sozio F, Schioppa T, Sozzani S, Del Prete A. Urethane-induced lung carcinogenesis. Methods Cell Biol 2021;163:45–57 [PubMed: 33785168]

9. Hwang I, Kim JW, Ylaya K, Chung EJ, Kitano H, Perry C, et al. Tumor-associated macrophage, angiogenesis and lymphangiogenesis markers predict prognosis of non-small cell lung cancer patients. J Transl Med 2020;18:443 [PubMed: 33228719]

10. Sedighzadeh SS, Khoshbin AP, Razi S, Keshavarz-Fathi M, Rezaei N. A narrative review of tumor-associated macrophages in lung cancer: regulation of macrophage polarization and therapeutic implications. Transl Lung Cancer Res 2021;10:1889–916 [PubMed: 34012800]

11. Melo EM, Oliveira VLS, Boff D, Galvao I. Pulmonary macrophages and their different roles in health and disease. Int J Biochem Cell Biol 2021;141:106095 [PubMed: 34653619]

12. Hou F, Xiao K, Tang L, Xie L Diversity of Macrophages in Lung Homeostasis and Diseases Front Immunol 2021; 24:12:753940.

13. Tan SYS, Krasnow MA Developmental origin of lung macrophage diversity Development. 2016. 15;143:1318–27.

14. Mass E, Ballesteros I, Farlik M, Halbritter F, Gunther P, Crozet L, et al. Specification of tissue-resident macrophages during organogenesis. Science 2016;353

15. Guilliams M, De Kleer I, Henri S, Post S, Vanhoutte L, De Prijck S, et al. Alveolar macrophages develop from fetal monocytes that differentiate into long-lived cells in the first week of life via GM-CSF. J Exp Med 2013;210:1977–92 [PubMed: 24043763]

16. Schneider C, Nobs SP, Kurrer M, Rehrauer H, Thiele C, Kopf M. Induction of the nuclear receptor PPAR-gamma by the cytokine GM-CSF is critical for the differentiation of fetal monocytes into alveolar macrophages. Nat Immunol 2014;15:1026–3 [PubMed: 25263125]

17. Kulikauskaite J, Wack A. Teaching Old Dogs New Tricks? The Plasticity of Lung Alveolar Macrophage Subsets. Trends Immunol 2020;41:864–77 [PubMed: 32896485]

18. Dehle FC, Mukaro VR, Jurisevic C, Moffat D, Ahern J, Hodge G, et al. Defective lung macrophage function in lung cancer +/− chronic obstructive pulmonary disease (COPD/emphysema)-mediated by cancer cell production of PGE2? PLoS One 2013;8:e61573 [PubMed: 23637858]

19. Senft D, Qi J, Ronai ZA. Ubiquitin ligases in oncogenic transformation and cancer therapy. Nat Rev Cancer 2018;18:69–88 [PubMed: 29242641]

20. Confalonieri S, Quarto M, Goisis G, Nuciforo P, Donzelli M, Jodice G, et al. Alterations of ubiquitin ligases in human cancer and their association with the natural history of the tumor. Oncogene 2009;28:2959–68 [PubMed: 19543318]

21. Qi J, Ronai ZA. Dysregulation of ubiquitin ligases in cancer. Drug Resist Updat 2015;23:1–11 [PubMed: 26690337]

22. Nakayama K, Frew IJ, Hagensen M, Skals M, Habelhah H, Bhoumik A, et al. Siah2 regulates stability of prolyl-hydroxylases, controls HIF1alpha abundance, and modulates physiological responses to hypoxia. Cell 2004;117:941–52 [PubMed: 15210114]

23. Scortegagna M, Kim H, Li JL, Yao H, Brill LM, Han J, Lau E, Bowtell D, Haddad G, Kaufman RJ, Ronai ZA.Fine tuning of the UPR by the ubiquitin ligases Siah1/2. 2014; PLoS Genet. 2014;10:e1004348. [PubMed: 24809345]

24. Qi J, Tripathi M, Mishra R, Sahgal N, Fazli L, Ettinger S, et al. The E3 ubiquitin ligase Siah2 contributes to castration-resistant prostate cancer by regulation of androgen receptor transcriptional activity. Cancer Cell 2013;23:332–46 [PubMed: 23518348]

25. Qi J, Nakayama K, Gaitonde S, Goydos JS, Krajewski S, Eroshkin A, Bar-Sagi D, Bowtell D, Ronai Z. The ubiquitin ligase Siah2 regulates tumorigenesis and metastasis by HIF-dependent and -independent pathways. Proc Natl Acad Sci U S A 2008;105:16713–8. [PubMed: 18946040]

26. Moreno P, Lara-Chica M, Soler-Torronteras R, Caro T, Medina M, Álvarez A, Salvatierra A, Muñoz E, Calzado MA. The Expression of the Ubiquitin Ligase SIAH2 (Seven In Absentia Homolog 2) Is Increased in Human Lung Cancer PLoS One. 2015; 10:e0143376. [PubMed: 26580787]

27. Müller S, Chen Y, Ginter T, et al. , SIAH2 antagonizes TYK2-STAT3 signaling in lung carcinoma cells Oncotarget. 2011;5:3184–96.

28. Li K, Li J, Ye M, Jin X The role of Siah2 in tumorigenesis and cancer therapy Gene. 2022; 809:146028. [PubMed: 34687788]

29. Xiao Z, Wei Z, Deng Z, et al. , Downregulation of Siah1 promotes colorectal cancer cell proliferation and migration by regulating AKT and YAP ubiquitylation and proteasome degradation Cancer Cell Int. 2020; 20:50. [PubMed: 32082080]

30. Roperch JP, Lethrone F, Prieur S, Piouffre L, Israeli D, Tuynder M, Nemani M, Pasturaud P, Gendron MC, Dausset J, Oren M, Amson RB, Telerman A. SIAH-1 promotes apoptosis and tumor suppression through a network involving the regulation of protein folding, unfolding, and trafficking: identification of common effectors with p53 and p21(Waf1) Proc Natl Acad Sci U S A.1999; ;96:8070–3. [PubMed: 10393949]

31. Scortegagna M, Hockemeyer K, Dolgalev I, Pozniak J, Rambow F, Li Y, et al. Siah2 control of T-regulatory cells limits anti-tumor immunity. Nat Commun 2020;11:99 [PubMed: 31911617]

32. Hu G, Chung YL, Glover T, Valentine V, Look AT, Fearon ER. Characterization of human homologs of the Drosophila seven in absentia (sina) gene. Genomics 1997;46:103–11 [PubMed: 9403064]

33. Martin M Cutadapt removes adapter sequences from high-throughput sequencing reads. EMBnetjournal 2011;v. 17:pp. 10–2

34. Dobin A, Davis CA, Schlesinger F, Drenkow J, Zaleski C, Jha S, et al. STAR: ultrafast universal RNA-seq aligner. Bioinformatics 2013;29:15–21 [PubMed: 23104886]

35. Li B, Dewey CN. RSEM: accurate transcript quantification from RNA-Seq data with or without a reference genome. BMC Bioinformatics. 2011;12:323. [PubMed: 21816040]

36. Ewels P, Magnusson M, Lundin S, Kaller M. MultiQC: summarize analysis results for multiple tools and samples in a single report. Bioinformatics 2016;32:3047–8 [PubMed: 27312411]

37. Love MI, Huber W, Anders S. Moderated estimation of fold change and dispersion for RNA-seq data with DESeq2. Genome Biol 2014;15:550 [PubMed: 25516281]

38. Frankish A, Diekhans M, Jungreis I, Lagarde J, Loveland JE, et al. , GENCODE 2021 Nucleic Acids Res. 2021; 49(D1):D916–D923. [PubMed: 33270111]

39. Butler A, Hoffman P, Smibert P, Papalexi E, Satija R. Share Integrating single-cell transcriptomic data across different conditions, technologies, and species. Nat Biotechnol. 2018; 36:411–420. [PubMed: 29608179]

40. Wickham H Data analysis. ggplot2: Springer; 2016. p 189–201.

41. Gu Z, Eils R, Schlesner M. Complex heatmaps reveal patterns and correlations in multidimensional genomic data Bioinformatics. 2016; 32:2847–9. [PubMed: 27207943]

42. Kim N, Kim HK, Lee K, Hong Y et al. Single-cell RNA sequencing demonstrates the molecular and cellular reprogramming of metastatic lung adenocarcinoma. Nat Commun 2020 May 8;11:2285 [PubMed: 32385277]

43. Korsunsky I, Millard N, Fan J, Slowikowski K, Zhang F, Wei K, et al. Fast, sensitive and accurate integration of single-cell data with Harmony. Nat Methods 2019;16:1289–96 [PubMed: 31740819]

44. Hoadley KA, Yau C, Hinoue T, Wolf DM, Lazar AJ, Drill E, et al. Cell-of-Origin Patterns Dominate the Molecular Classification of 10,000 Tumors from 33 Types of Cancer. Cell 2018;173:291–304 e6 [PubMed: 29625048]

45. Therneau TM, and Grambsch PM. . Modeling Survival Data: Extending the Cox Model. New York: Springer-Verlag 2000.

46. Kassambara A, Kosinski M, Biecek P, Fabian S. Package 'survminer'. Drawing Survival Curves using 'ggplot2'(R package version 03 1) 2017

47. Hothorn T, Hothorn MT, Suggests T. Package 'maxstat'. 2017

48. Kun Wang SP, Joo Sang Lee, E. Michael Gertz, Welles Robinson, Fiorella Schischlik, David R. Crawford, Alejandro A. Schäffer, Eytan Ruppin. Deconvolving clinically relevant cellular immune crosstalk from bulk gene expression using CODEFACS and LIRICS. 2021.

49. Gal-Oz ST, Maier B, Yoshida H, Seddu K, Elbaz N, Czysz C, et al. ImmGen report: sexual dimorphism in the immune system transcriptome. Nat Commun 2019;10:4295 [PubMed: 31541153]

50. Gibbings SL, Thomas SM, Atif SM, McCubbrey AL, Desch AN, Danhorn T, et al. Three Unique Interstitial Macrophages in the Murine Lung at Steady State. Am J Respir Cell Mol Biol 2017;57:66–76 [PubMed: 28257233]

51. Misharin AV, Morales-Nebreda L, Reyfman PA, Cuda CM, Walter JM, McQuattie-Pimentel AC, et al. Monocyte-derived alveolar macrophages drive lung fibrosis and persist in the lung over the life span. J Exp Med 2017;214:2387–404 [PubMed: 28694385]

52. Kasembeli MM, Bharadwaj U, Robinson P, Tweardy DJ. Contribution of STAT3 to Inflammatory and Fibrotic Diseases and Prospects for its Targeting for Treatment. Int J Mol Sci 2018;19

53. Pechkovsky DV, Prasse A, Kollert F, Engel KM, Dentler J, Luttmann W, et al. Alternatively activated alveolar macrophages in pulmonary fibrosis-mediator production and intracellular signal transduction. Clin Immunol 2010;137:89–101 [PubMed: 20674506]

54. Sennello JA, Misharin AV, Flozak AS, Berdnikovs S, Cheresh P, Varga J, et al. Lrp5/beta-Catenin Signaling Controls Lung Macrophage Differentiation and Inhibits Resolution of Fibrosis. Am J Respir Cell Mol Biol 2017;56:191–201 [PubMed: 27668462]

55. Huang R, Wang S, Wang N, Zheng Y, Zhou J, Yang B, et al. CCL5 derived from tumor-associated macrophages promotes prostate cancer stem cells and metastasis via activating beta-catenin/STAT3 signaling. Cell Death Dis 2020;11:234 [PubMed: 32300100]

56. Rosenbloom AB, Tarczynski M, Lam N, Kane RS, Bugaj LJ, Schaffer DV. beta-Catenin signaling dynamics regulate cell fate in differentiating neural stem cells. Proc Natl Acad Sci U S A 2020;117:28828–37 [PubMed: 33139571]

57. Gurley KE, Moser RD, Kemp CJ. Induction of Lung Tumors in Mice with Urethane. Cold Spring Harb Protoc 2015;2015:pdb prot077446

58. Xie N, Cui H, Ge J, Banerjee S, Guo S, Dubey S, et al. Metabolic characterization and RNA profiling reveal glycolytic dependence of profibrotic phenotype of alveolar macrophages in lung fibrosis. Am J Physiol Lung Cell Mol Physiol 2017;313:L834–L44 [PubMed: 28798256]

59. Wang W, Guo H, Geng J, Zheng X, Wei H, Sun R, et al. Tumor-released Galectin-3, a soluble inhibitory ligand of human NKp30, plays an important role in tumor escape from NK cell attack. J Biol Chem 2014;289:33311–9 [PubMed: 25315772]

60. Farhad M, Rolig AS, Redmond WL. The role of Galectin-3 in modulating tumor growth and immunosuppression within the tumor microenvironment. Oncoimmunology 2018;7:e1434467 [PubMed: 29872573]

61. Zhou HC , Yan XY, Yu WW, Liang XQ, Du XY, et al. Lactic acid in macrophage polarization: The significant role in inflammation and cancer. Int Rev Immunol. 2022; 41:4–18 [PubMed: 34304685]

62. Afik R, Zigmond E, Vugman M, Klepfish M, Shimshoni E, et al. , Tumor macrophages are pivotal constructors of tumor collagenous matrix. J Exp Med. 2016; 213:2315–2331. [PubMed: 27697834]

63. Wang Z, Li Z, Zhou K, Wang C, Jiang L, Zhang L, et al. Deciphering cell lineage specification of human lung adenocarcinoma with single-cell RNA sequencing. Nat Commun 2021;12:6500 [PubMed: 34764257]

64. Morgan AJ, Guillen C, Symon FA, Huynh TT, Berry MA, Entwisle JJ, et al. Expression of CXCR6 and its ligand CXCL16 in the lung in health and disease. Clin Exp Allergy 2005;35:1572–80 [PubMed: 16393323]

65. Binnewies M, Pollack JL, Rudolph J, Dash S, Abushawish M, Lee T, et al. Targeting TREM2 on tumor-associated macrophages enhances immunotherapy. Cell Rep 2021;37:109844 [PubMed: 34686340]

66. Shi Q, Shen Q, Liu Y, Shi Y, Huang W, Wang X, et al. Increased glucose metabolism in TAMs fuels O-GlcNAcylation of lysosomal Cathepsin B to promote cancer metastasis and chemoresistance. Cancer Cell 2022;40:1207–22 e10 [PubMed: 36084651]

67. Reyfman PA, Walter JM, Joshi N, Anekalla KR, McQuattie-Pimentel AC, Chiu S, et al. Single-Cell Transcriptomic Analysis of Human Lung Provides Insights into the Pathobiology of Pulmonary Fibrosis. Am J Respir Crit Care Med 2019;199:1517–36 [PubMed: 30554520]

68. Lee SJ, Lee J, Park YS, Lee CH, Lee SM, Yim JJ, et al. Impact of smoking on mortality of patients with non-small cell lung cancer. Thorac Cancer 2014;5:43–9 [PubMed: 26766971]

69. Yu X, Buttgereit A, Lelios I, Utz SG, Cansever D, Becher B, et al. The Cytokine TGF-beta Promotes the Development and Homeostasis of Alveolar Macrophages. Immunity 2017;47:903–12 e4 [PubMed: 29126797]

70. Gao H, Guo RF, Speyer CL, Reuben J, Neff TA, Hoesel LM, et al. Stat3 activation in acute lung injury. J Immunol 2004;172:7703–12 [PubMed: 15187153]

71. Shin M, Yi EH, Kim BH, Shin JC, Park JY, Cho CH, et al. STAT3 Potentiates SIAH-1 Mediated Proteasomal Degradation of beta-Catenin in Human Embryonic Kidney Cells. Mol Cells 2016;39:821–6 [PubMed: 27871173]

72. Matsuzawa SI, Reed JC. Siah-1, SIP, and Ebi collaborate in a novel pathway for beta-catenin degradation linked to p53 responses. Mol Cell 2001;7:915–26 [PubMed: 11389839]

73. Ma B, Chen Y, Chen L, Cheng H, Mu C, Li J, et al. Hypoxia regulates Hippo signalling through the SIAH2 ubiquitin E3 ligase. Nat Cell Biol 2015;17:95–103 [PubMed: 25438054]
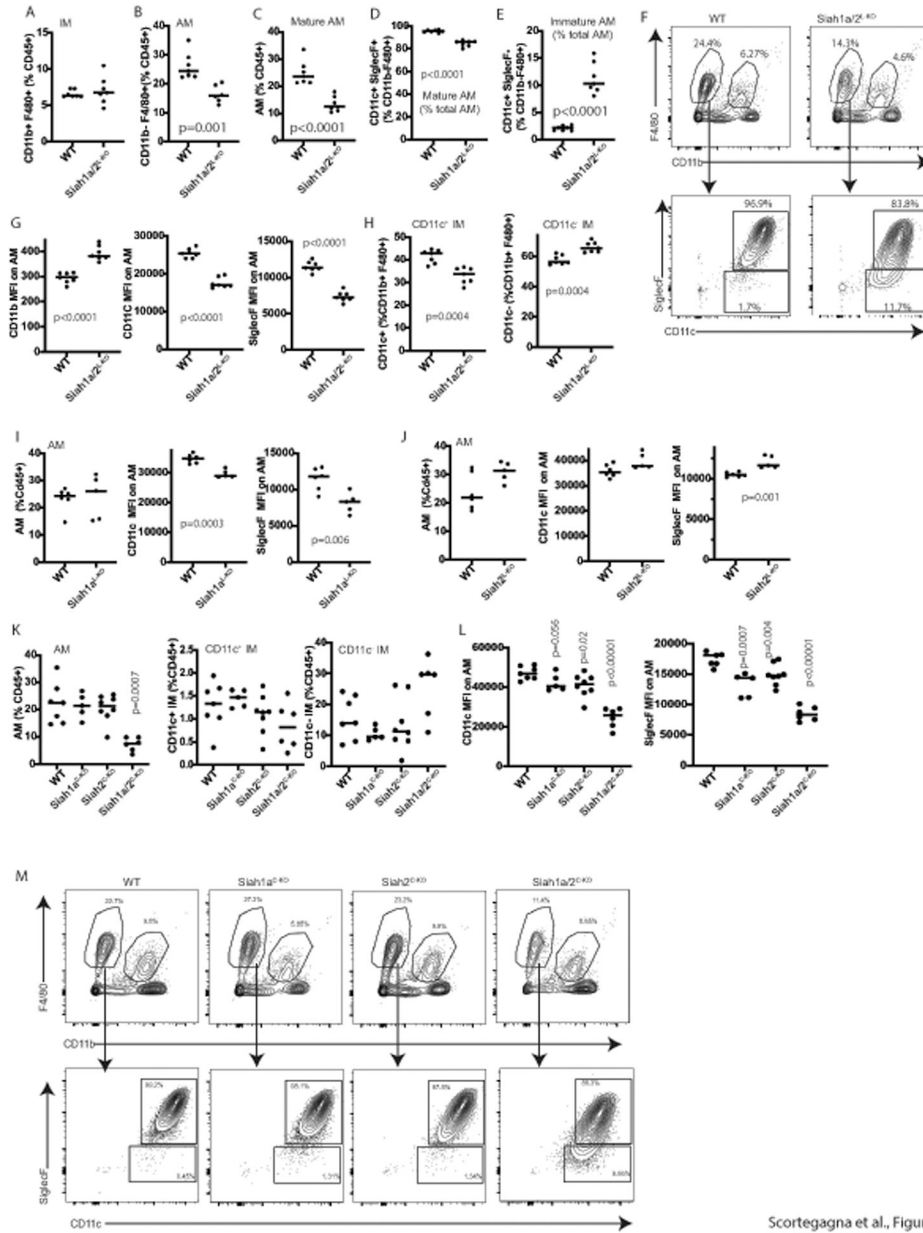
Significance

The ubiquitin ligases Siah1a/2 control proinflammatory signaling, differentiation, and pro-fibrotic phenotypes of alveolar macrophages to suppress lung carcinogenesis.

Figure 1. Siah1a and Siah2 are required for AM terminal differentiation and maturation.
A–C, Frequency of (A) interstitial macrophages (IMs: CD11b$^+$ F4/80$^+$), (B) total alveolar
macrophages (AMs: CD11b$^{low/neg}$ F4/80$^+$), and (C) mature AMs (CD11b$^{low/neg}$ F4/80$^+$
CD11c$^+$ SiglecF$^+$) among CD45$^+$ cells in lungs of WT and *Siah1a/2$^{f/f}$::Lyz2^{Cre}* (*Siah1a/
2^{L-KO}*) mice (n=7). **D, E,** Frequency of (D) mature AMs and (E) immature AMs
(CD11c$^+$ SiglecF^{low}) among total AMs in lungs of WT and *Siah1a/2^{L-KO}* mice (n=7).
F, Representative FACS analysis plots showing selection of gated CD11c$^+$ SiglecF$^+$ cells
(1.7% *vs* 11.7%) among the CD45.2$^+$ CD11b^{low} F4/80$^+$ cell population in lungs of WT
and *Siah1a/2^{L-KO}* mice. **G,** Expression levels (mean fluorescence intensity, MFI) of CD11b,
CD11c, and SiglecF on CD45.2$^+$ mature AMs (CD11b$^{low/neg}$ F4/80$^+$ CD11c$^+$ SiglecF$^+$) in
lungs of WT and *Siah1a/2^{L-KO}* mice (n=7). **H,** Frequency of CD11c$^+$ and CD11c$^-$ cells

among CD45.2^{+} IMs (CD11b^{+} F4/80^{+}) in lungs of WT and *Siah1a/2*[L-KO] mice cells (n=7). **I, J,** Frequency of CD45.2^{+} AMs (CD11b[low/neg] F4/80^{+}) and MFI of CD11c and SiglecF expressed on AMs in the lungs of WT (n=6), *Siah1a*[L-KO] (I, n=5) or *Siah2*[L-KO] (J, n=5) mice. **K,** Frequency of CD45.2^{+} AMs, CD11c^{+} IMs, and CD11c^{−} IMs in lungs of WT (n=7), *Siah1a*[C-KO] (n=5), *Siah1a/2*[C-KO] (n=6), and *Siah2*[C-KO] (n=8) mice. **L,** MFI of CD11c and SiglecF on mature AMs (CD45.2^{+} CD11b^{low} F4/80^{+} CD11c^{+} SiglecF^{+} cells) in lungs of WT (n=7), *Siah1a*[C-KO] (n=5), *Siah2*[C-KO] (n=8), and *Siah1a/2*[C-KO] (n=6) mice. **M,** Representative FACS plots showing relative frequency of CD11c^{+} SiglecF^{+} or CD11c^{+} SiglecF[low/neg] cells among total CD45.2^{+} AMs in lungs of WT and *Siah1a*[C-KO], *Siah2*[C-KO], and *Siah1a/2*[C-KO] mice. Data were analyzed by unpaired t-test.
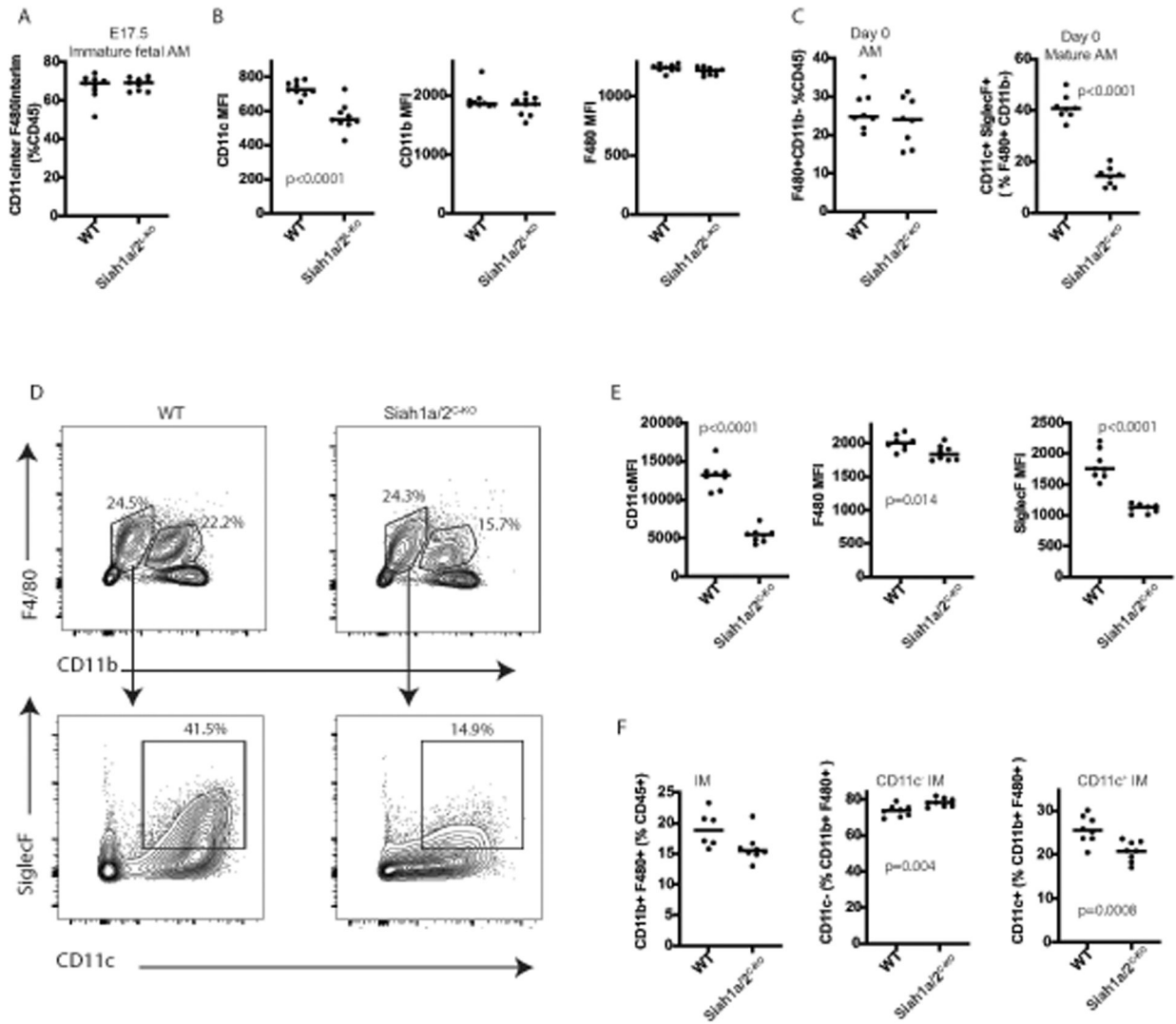
Figure 2. Siah1a and Siah2 regulate maturation of fetal monocytes to AMs.
A, B, Frequency of fetal immature AMs with intermediate expression of (A) CD11c and F4/80 among total CD45.2$^+$ cells and expression levels (mean fluorescence intensity, MFI) of (B) CD11c, CD11b, and F4/80 on fetal immature AMs from E17.5 lungs of WT and *Siah1a/2*$^{L-KO}$ embryos (n=9). **C,** Frequency of F4/80$^+$ CD11b^{low} cells among CD45$^+$ cells and of CD11c$^+$ SiglecF$^+$ cells among F4/80$^+$ CD11b^{low} cells from lungs of WT (n=8) and *Siah1a/2*$^{C-KO}$ neonates (Day 0, n=8). **D,** Representative flow cytometry plots depicting frequency of CD11c$^+$ SiglecF$^+$ cells in a gated subpopulation of CD45.2$^+$ CD11b^{low} F4/80$^+$ cells from lungs of WT and *Siah1a/2*$^{L-KO}$ mice (n=8). **E.** Expression levels (mean fluorescence intensity, MFI) of CD11c, F4/80, and SiglecF on AMs (CD11b^{low} F4/80$^+$ SiglecF$^+$ CD11c$^+$) from lungs of WT (n=8) and *Siah1a/2*$^{C-KO}$ neonates (Day 0, n=8). **F,** Frequency of IMs (F4/80$^+$ CD11b$^+$) among CD45$^+$ cells and of CD11c$^+$ IMs and CD11c$^-$ IMs among IMs from lungs of WT (n=8) and *Siah1a/2*$^{C-KO}$ neonates (Day 0, n=8). Data were analyzed by unpaired t-test.
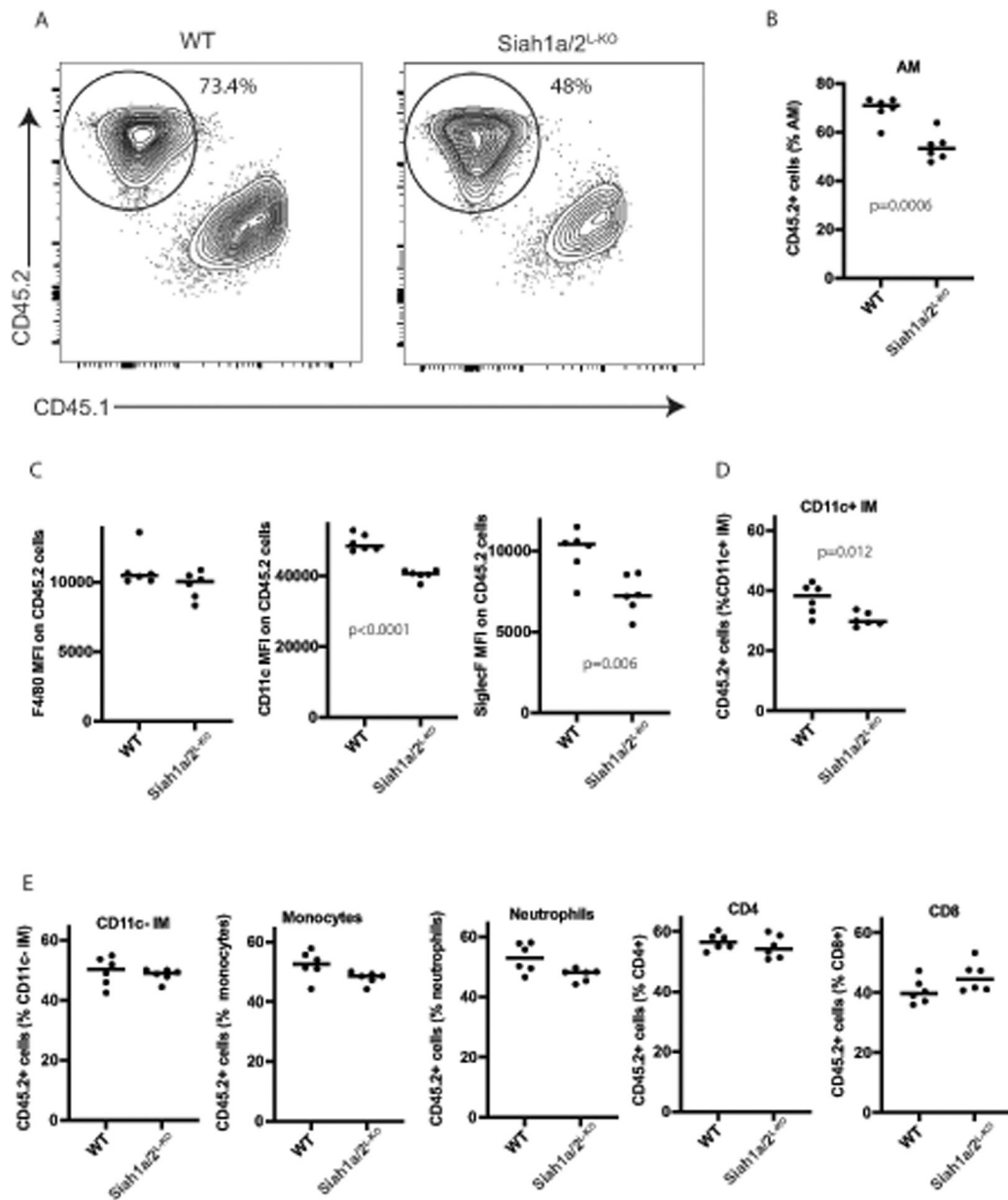
Figure 3. AM regeneration from bone marrow requires Siah1a and Siah2.
Bone marrow cells from CD45.2+ *Siah1a/2*[L-KO] or CD45.2+ WT mice were co-transplanted (at a 1:1 ratio) with CD45.1+ bone marrow cells into lethally-irradiated C57BL/6 mice, and lungs were harvested 10 weeks later. **A**, **B**, Representative FACS plots (A) and quantitation (B) of CD45.2+ mature AMs (CD11b^{low} F4/80+ CD11c+ SiglecF+) from mice reconstituted with either *Siah1a/2*[L-KO] or WT CD45.2+ cells. **C**, Mean fluorescence intensity (MFI) of F4/80, CD11c, and SiglecF on CD45.2+ mature AMs from mice reconstituted as described for (A, B). **D**, Frequency of CD45.2+ CD11c+ IMs (CD11b+ F4/80+ CD11c+) from mice reconstituted as described for (A, B). **E**, Frequency of CD45.2+ CD11c− IMs (CD11b+ F4/80+ CD11c−), monocytes (CD11b+ Ly6C+), neutrophils (CD11b+ Ly6G+), and CD4+

or CD8$^+$ T cells from mice reconstituted as described for (A, B). N=6 mice/group for all analyses. Data were analyzed by unpaired t-test.
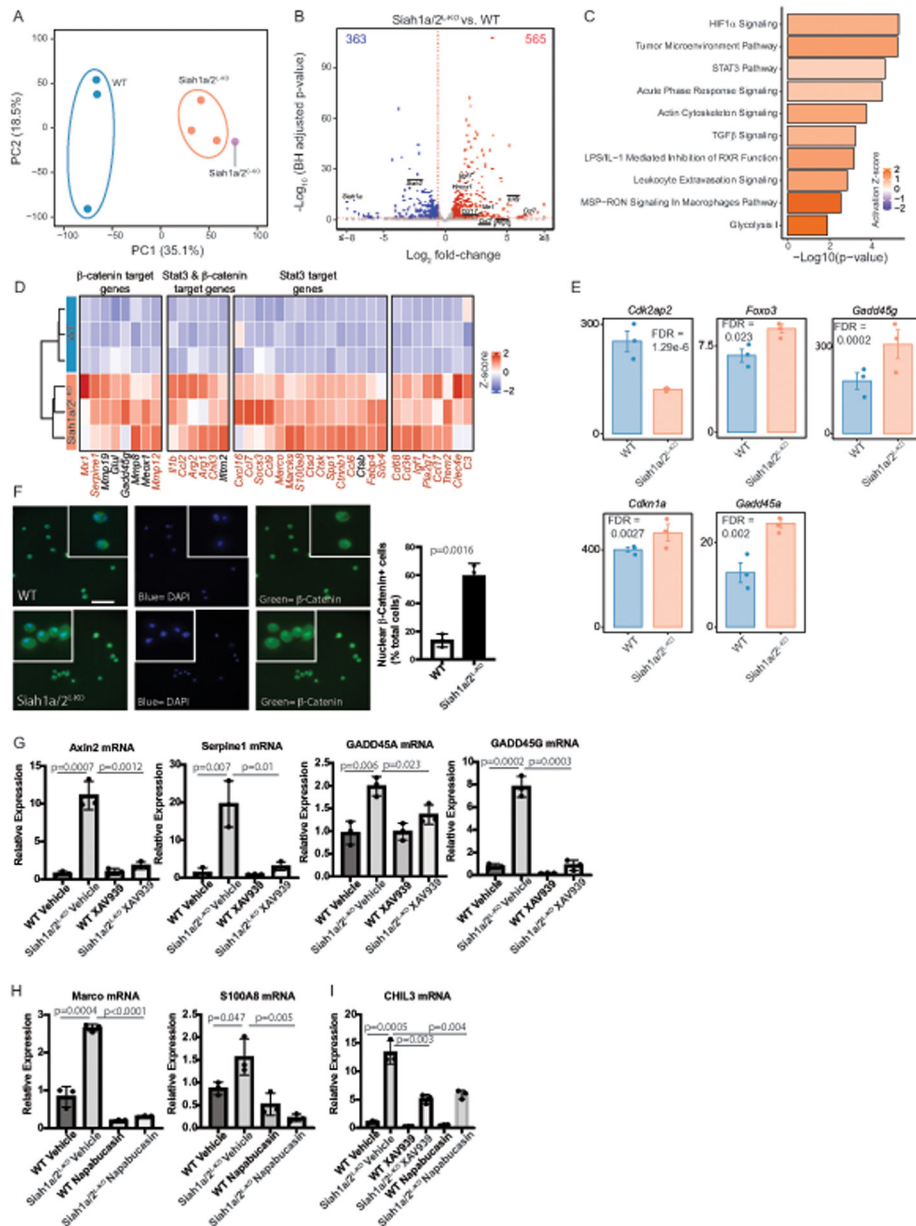
Figure 4. Siah1a and Siah2 control AM immunoregulatory function.

RNA-seq analysis of CD45$^+$ CD11c$^+$ F4/80$^+$ SiglecF$^+$ cells sorted from lungs of WT (n=3), *Siah1a/2*$^{L-KO}$ (n=3), or *Siah1a/2*$^{C-KO}$ (n=1) mice. Each sample was a pool of 3 lungs. **A,** Principal component analysis (PCA) plot based on gene expression. **B,** Volcano plot of genes differentially expressed in KO *vs* WT lungs. Selected upregulated and downregulated genes are labeled. **C,** Activation z-scores and significance p values of the most upregulated pathways in *Siah1a/2*$^{L-KO}$ *vs* WT AMs. **D–E,** Heatmaps and bar charts showing z-scores for expression of indicated genes associated with (D) inflammation and (E) the cell cycle from WT and *Siah1a/2*$^{L-KO}$ AMs. Genes highlighted in red are genes associated with fibrosis. **F,** Immunofluorescence staining of β-catenin (green, left) and quantitation of β-catenin$^+$ cells (right) among primary AMs cultured overnight with GM-CSF. Nuclei were stained

with DAPI (blue). N=3. Scale bar, 600 μM. **G-I,** qRT-PCR analysis of indicated mRNAs in primary AMs cultured for 6 days and treated overnight with vehicle, the β-catenin inhibitor XAV939 (G and I) or the Stat3 inhibitor Napabucasin (H and I). N=3. Data were analyzed by unpaired t-test (F-I) or the Wade test (E).
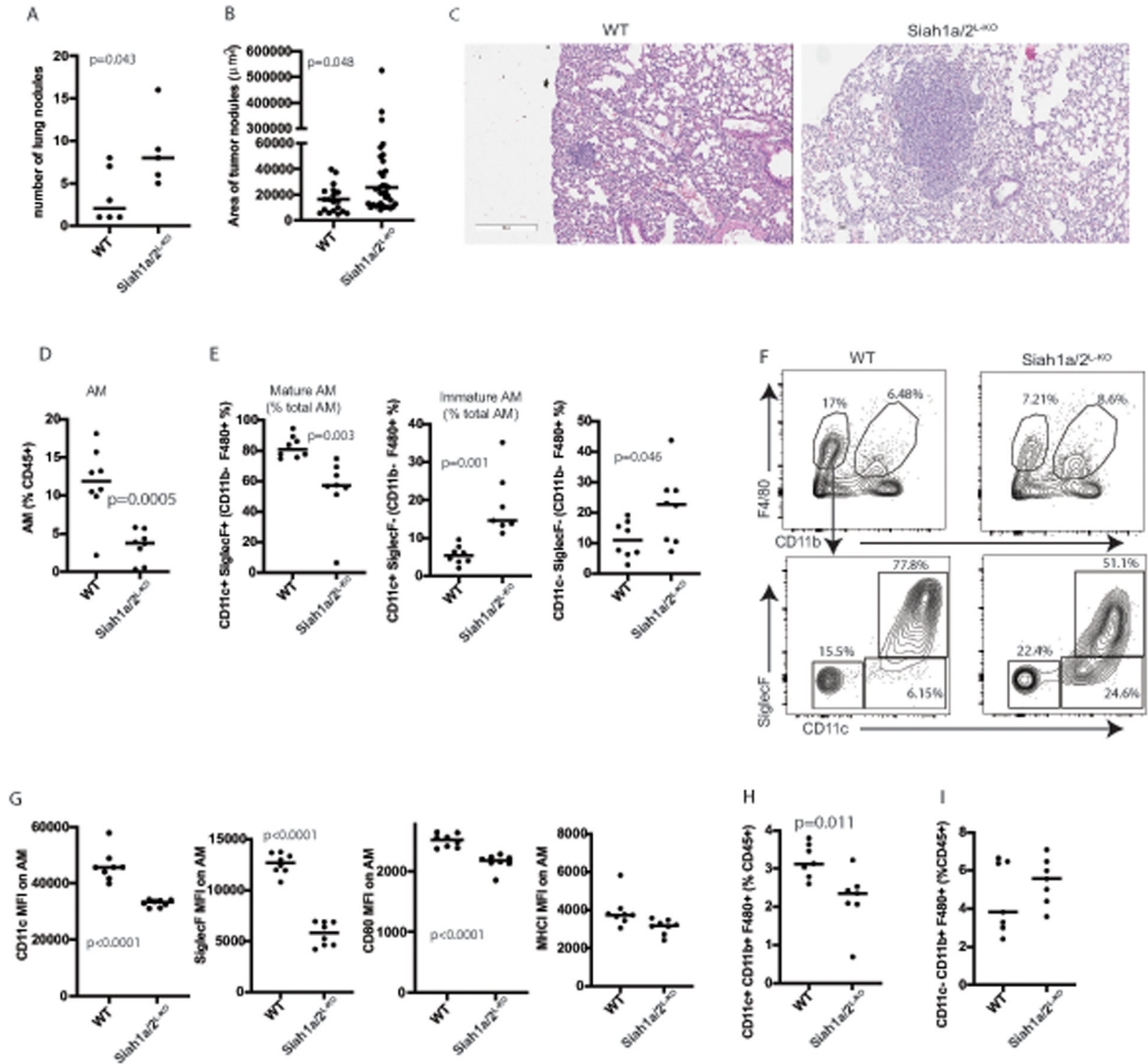
Figure 5. Macrophage-specific *Siah1a/2* deletion promotes exacerbates urethane-induced lung cancer.

Mice were injected intraperitoneally with urethane (1 mg/g body weight) once a week for 6 weeks, and lungs were collected 22 weeks after the first injection. All panels compare urethane-treated mice. A, B, (A) Number and (B) size of tumor nodules quantified by H&E staining of lung sections [WT mice (n=6) showed total of 21 tumors, whereas *Siah1a/2*[L-KO] mice (n=5) showed total of 44 tumors]. C, Representative H&E-stained lung sections. Scale bar, 300 μM. D, AM frequencies among total CD45+ lung cells (n=8). E, Frequencies of mature (CD11c+ SiglecF+) and immature (CD11c+ or CD11c− SiglecF−) cells among CD11b^{low} F4/80+ AMs (n=8). F, Representative FACS plots showing frequency of CD11c+ SiglecF+ cells in a gated subpopulation of CD45.2+ CD11b^{low} F4/80+ lung cells. G, Mean fluorescence intensity (MFI) of CD11c, SiglecF, CD80, and MHCI on mature CD45.2+ AMs (CD11b^{low} F4/80+ CD11c+ SiglecF+). H, I, Frequencies of (H) CD11c+ and (I) CD11c− CD45+ IMs in lungs (n=8). Data were analyzed by unpaired t-test.
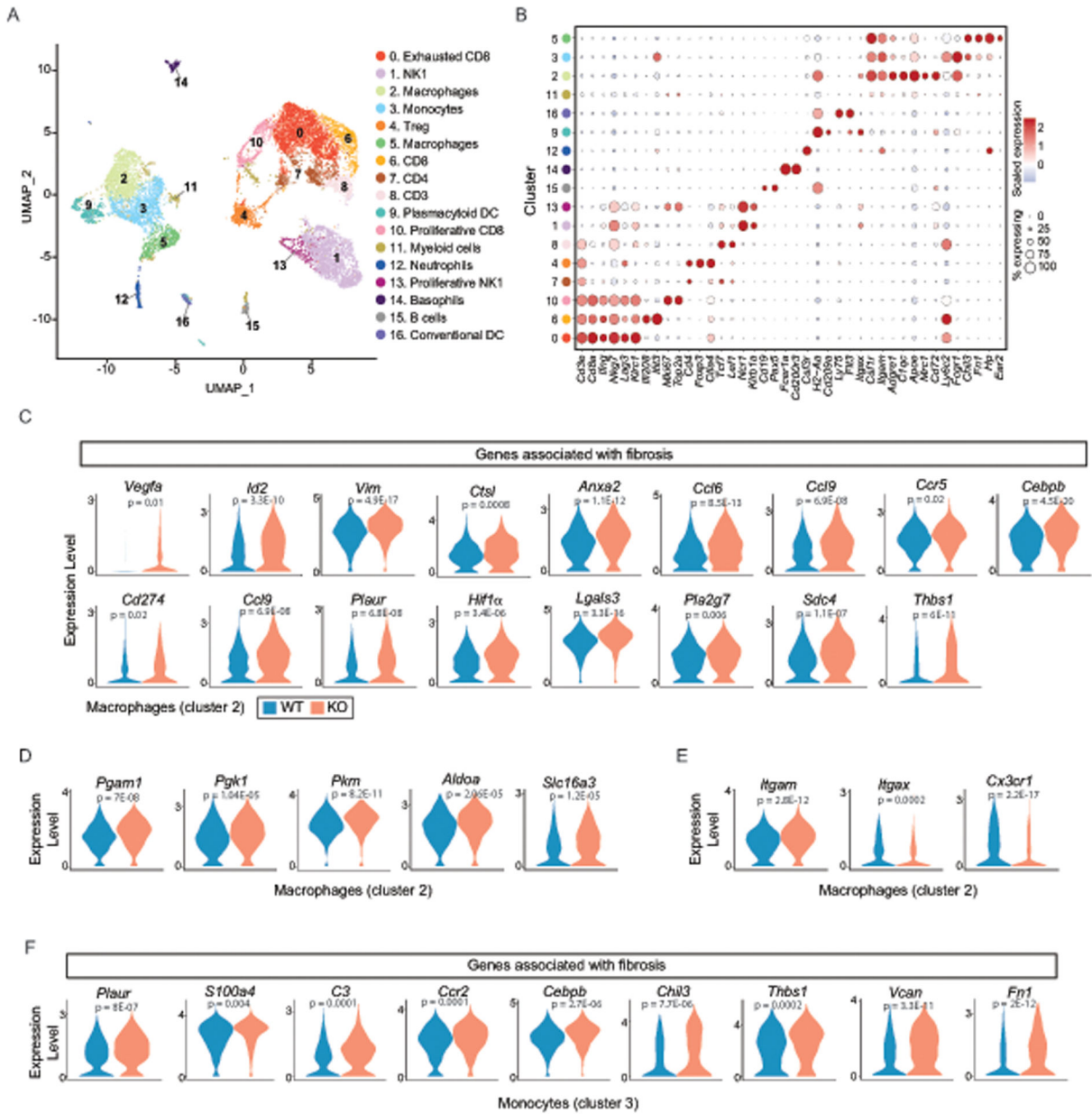
Figure 6. Macrophage-specific *Siah1a/2* deletion prevents maturation and induces an immunoregulatory/pro-fibrotic phenotype in select macrophage clusters.

WT and *Siah1a/2*[L-KO] mice were injected intraperitoneally with urethane (1 mg/g body weight) once a week for 6 weeks, and lungs were collected 1 week after the last injection. Lung CD45^{+} cells were sorted and single-cell RNA-seq was performed. All panels compare urethane-treated mice. **A,** UMAP plot of CD45^{+} cells from WT (n=7884 cells) and *Siah1a/2*[L-KO] (n=6035 cells) lungs showing 17 distinct clusters. Immune cell types identified using expression of specific markers are labeled. **B,** Scaled expression levels of selected markers used to identify cell clusters in (A). **C–E,** Violin plots comparing expression of genes in macrophages (cluster 2) (C) associated with fibrosis, (D) involved in glycolysis, or (E) involved in macrophage differentiation. **F,** Violin plots comparing expression of genes in

monocytes (cluster 3) associated with fibrosis. Data were analyzed using *FindMarkers()* and *MAST* test in Seurat.
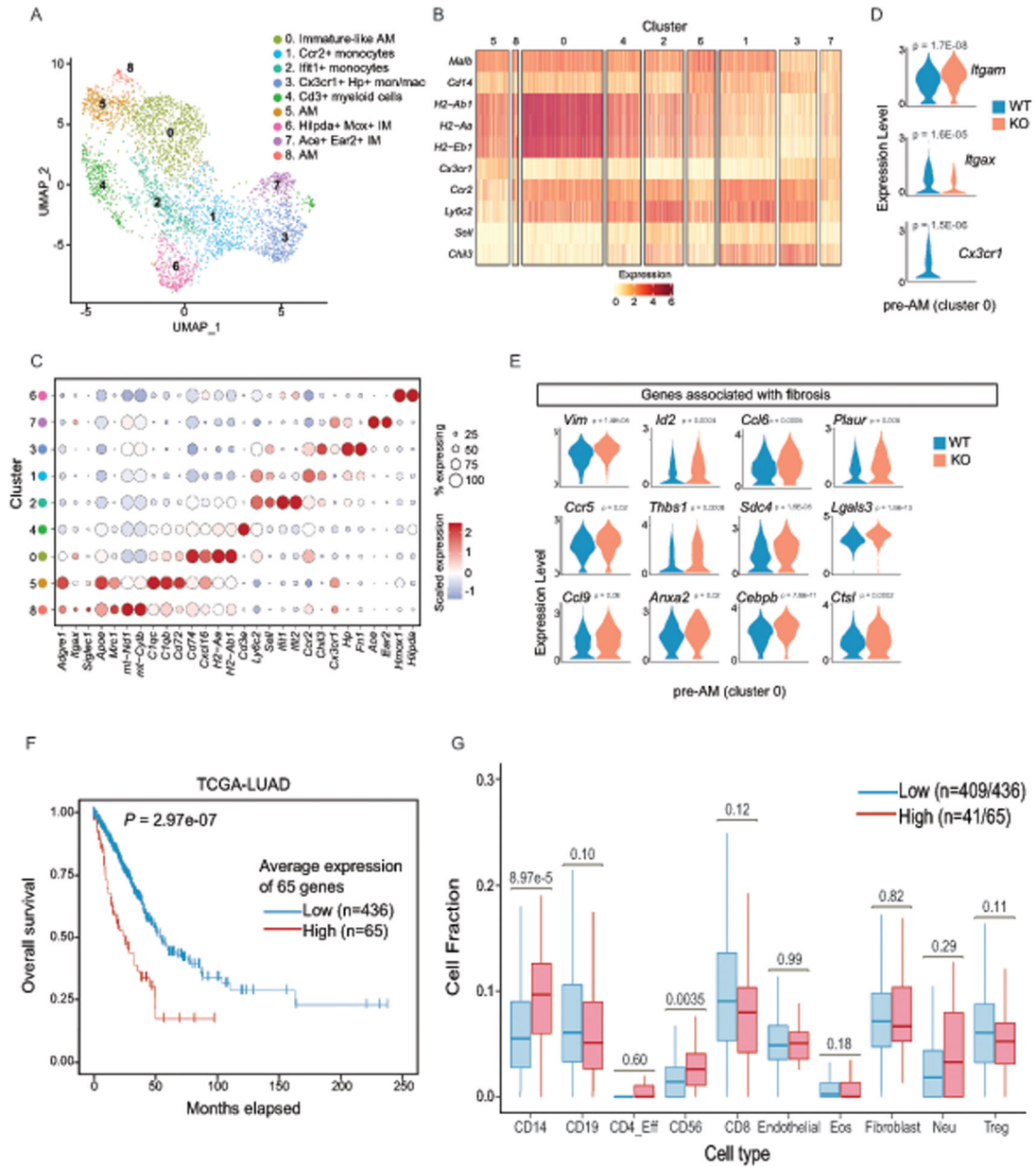
Figure 7. Macrophage-specific *Siah1a/2* deletion promotes an immunoregulatory/pro-fibrotic phenotype in monocyte-derived AMs.
Myeloid cell clusters (2, 3, and 5) from the global UMAP in Fig. 6A were re-clustered to obtain higher resolution clustering of myeloid cells. **A,** UMAP plot of re-clustered myeloid cells from lungs of WT (n=2245 cells) and *Siah1a/2*L-KO (n=1417 cells) mice showing 9 distinct clusters. **B,** Heat map of expression levels of markers of monocytic origin in each myeloid cell cluster. **C,** Dot plots showing scaled expression of marker genes used to identify specific subclusters of myeloid cells. **D, E,** Violin plots comparing expression of genes in subcluster 0 (D) functioning in AM differentiation and (E) associated with fibrosis. **F,** Kaplan–Meier survival curves for a TCGA-LUAD dataset of patients stratified on the basis of high (n=65) or low (n=436) average expression of 62 upregulated genes detected in subcluster 0 cells from KO *vs* WT mouse lungs. **G,** Cell composition of TCGA-LUAD

patient tumors was assessed using cell-type and gene-expression deconvolution datasets from CODEFACS. Patients were stratified as described in (F). Data were analyzed using *FindMarkers* and *MAST* test in Seurat (D, E) and the Wilcoxon rank sum test (F).
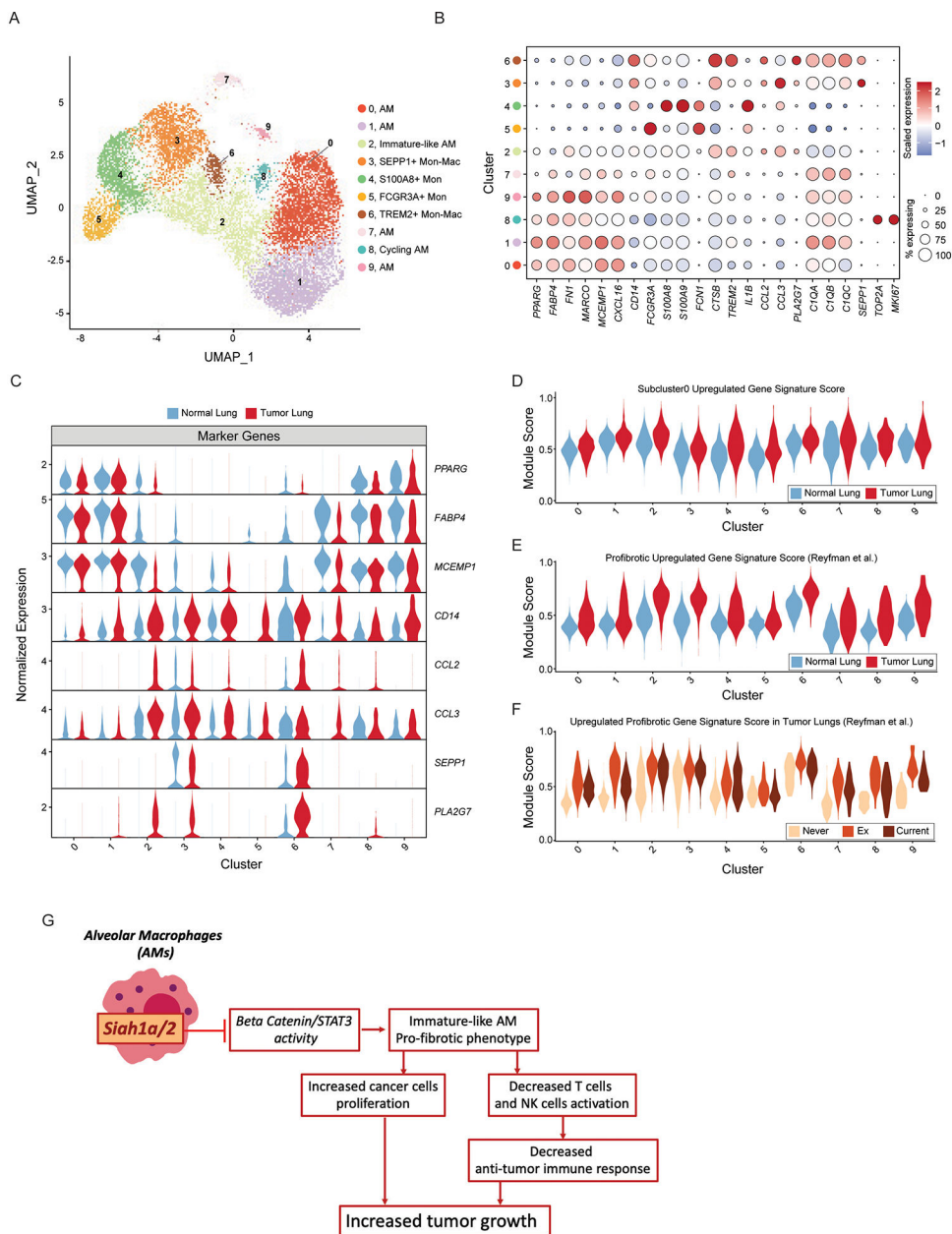
Figure 8. LUAD tumors exhibit expansion of an immature AM cluster marked by pro-fibrotic phenotypes.

Monocyte and macrophage clusters from single-cell RNA-seq analysis of patient lung tissue were re-clustered to obtain higher resolution clustering of myeloid cells. **A,** Integrated UMAP plot of monocytes and macrophages from normal lung (n=15,338 cells) and tumor (n=6641 cells) tissue showing 10 distinct clusters. **B,** Dot plots showing scaled expression of marker genes used to identify specific subclusters of myeloid cells. **C,** Violin plots comparing expression of selected genes from all subclusters in normal lung and tumor tissues. **D** Violin plots showing average expression of the 65-gene signature (identified in mouse subcluster 0 of *Siah1a/2*[L-KO] *vs* WT) in monocyte/macrophage clusters of lung tissue from LUAD patients. **E, F,** Violin plots showing average expression of a pro-fibrotic gene

signature (identified in AMs of patients with pulmonary fibrosis) in monocyte/macrophage clusters of lung tissue from (E) LUAD patients and (F) LUAD patients who were current, ex- or never-smokers. Data were analyzed using *FindMarkers()* and *MAST* test in Seurat. **G**, Proposed model showing Siah1a/2-dependent signaling pathways in AMs and their role in lung cancer progression.